Chapter 7
A Levelset-Based Sharp-Interface Modified Ghost Fluid Method for High-Speed Multiphase Flows and Multi-Material Hypervelocity Impact

Pratik Das, Nirmal K. Rai, and H. S. Udaykumar

7.1 Introduction

The dynamic response of multi-material interfaces under high-speed flow conditions is important in a wide variety of engineering applications. For example, the interaction between gas–liquid interfaces and high-speed flows plays an important role in underwater explosions and droplet combustion in gas-turbine engines and rocket motors (Powell et al. 2001; Mayer and Tamura 1996). Shock interaction with gas–solid interfaces is important in shock-induced dispersal of granular material after explosions (Boiko et al. 1997), high-speed coating technologies (Dongmo et al. 2008), shock processing of powders (Thadhani 1988), shock wave lithotripsy (Jamaluddin et al. 2011), etc. The hypervelocity interaction between two solid interfaces is important in the high-speed impact penetration scenarios seen during high-velocity machining processes (Marusich and Ortiz 1995), high-velocity geological impacts (Artemieva and Shuvalov 2008), and munition–target interaction (Bürger et al. 2012). In such high-speed multi-material flow problems, severe topological change of the multi-material interfaces can occur. The interfaces may suffer extreme deformation (high-speed machining), fragmentation (droplet break-up), and collapse (shock-induced bubble or void collapse in solid or liquid); new interfaces can be created (cavitation in liquid or damage in solid material). The situation is further complicated by the interaction of high-speed nonlinear waves (e.g., shocks, tensile waves, or detonation fronts) in the material with the interfaces. The complex physics associated with the interfacial dynamics makes compressible multi-material flow problems numerically challenging. In this chapter, we describe a generic numerical framework for solving problems involving the interaction of multi-material interfaces with high-speed flows.

P. Das · N. K. Rai · H. S. Udaykumar (✉)
Department of Mechanical Engineering, The University of Iowa, Iowa City, IA, USA
e-mail: hs-kumar@uiowa.edu

Numerical methods for solving high-speed multi-material flow problems are broadly classified under two approaches: Lagrangian and Eulerian. Lagrangian approaches are popular for solving high-speed multi-material flow problems, especially in solid mechanics. The computational mesh in Lagrangian methods follows the material points. In high-strain rate problems, extreme deformation of the material may cause entanglement of the initial Lagrangian mesh and frequent re-meshing may be required, which renders the numerical solution of such problems computationally challenging. The numerical challenges of mesh entanglement with large deformation in the Lagrangian methods are ameliorated to some extent in the arbitrary Lagrangian–Eulerian (ALE) methods. In the ALE method, the mesh conforms to the contours of the deforming object, but the mesh is not attached to the material points. Nonetheless, re-meshing is still required in ALE to handle large deformation of interfaces and objects in high-speed flow problems. An alternative approach for such problems is the Eulerian method. In the Eulerian frameworks, the mesh is fixed, and the material is allowed to "flow through" the mesh. Eulerian formulations are preferred for solving problems in fluid mechanics, but the Eulerian framework can also be used to solve the high-speed problems in solid mechanics. In the Eulerian formulations for solid mechanics, spurious elastic dissipation may occur as the elastic part of strain is not fully recovered because of nonintegrability in the elasticity model. Nevertheless, under high-strain rate conditions, the elastic strains are negligible compared to the plastic strain. Furthermore, a unifying feature of broad spectrum of problems under high-speed and/or high-strain rate conditions is the hyperbolic nature of the governing equations, which can be cast under the umbrella of a general Eulerian framework.

In the fixed-grid Eulerian methods, there is no explicit definition of the interfaces between different materials or phases. The interfaces do not align with the fixed background mesh; instead, the interfaces are embedded in the fixed-grid. The interfaces are tracked implicitly either through a progress variable/field variable or Lagrangian marker point. For example, the levelset methods (Osher and Sethian 1988; Sethian and Smereka 2003; Sussman et al. 1998) uses a signed distance field on the Eulerian grid to track the evolution of the interface. Similarly, in the volume of fluid method (VOF) (Hirt and Nichols 1981), a marker function is defined as the volume of a certain phase at a given computational cell of the Eulerian grid to keep track of the interfaces. The front tracking methods (Unverdi and Tryggvason 1992) use Lagrangian marker points to trace the location of the interfaces embedded within the Eulerian grid. Among these methods, levelset-based sharp-interface tracking methods are attractive for solving high-speed multi-material flow problems. In the levelset-based approach, zero-levelset contours sharply define the interfaces embedded in the background mesh. Therefore, in the levelset-based approach, the definition of the sharp interface is readily available from the levelset field, whereas, in VOF or front tracking methods, the sharp interface is reconstructed from the volume fraction field or the Lagrangian marker points, respectively. Also, with the levelset-based approach, the extreme deformation, collision, merging, and fragmentation of the interface is naturally incorporated through the advection of the levelset

field. Therefore, levelset-based sharp-interface tracking is attractive for high-speed multi-material flows where extreme deformation of the interfaces is commonplace.

The major challenges of Eulerian sharp-interface methods lie in applying boundary conditions at the interfaces because in such methods the embedded interface does not align with the background mesh. The ghost fluid method (GFM), originally developed by Fedkiw et al. (1999), has been successfully used to prescribe appropriate boundary conditions at the embedded interfaces. In the GFM approach (Sambasivan and UdayKumar 2009; Shiv Kumar and UdayKumar 2009), a band of computational cells around the interface is defined as ghost points corresponding to each phase of the interacting media. The ghost band, when supplied with appropriate flow conditions, together with the respective real fluid, constitutes a single flow field. The success of the GFM approach largely depends on the accuracy with which the ghost states are populated. The ghost states, in turn, are derived based on the material enclosed by the embedded interfaces. Thus, in the GFM framework, the treatment of embedded interfaces essentially boils down to suitably defining the ghost states such that the material properties and the interface conditions are represented accurately. The interfacial conditions imposed at the interface through the GFM depends on the materials/phases separated by the interfaces. The numerical implementations of the interfacial conditions for different multi-material interfaces are discussed in this chapter.

In the following sections of this chapter, first, the unified governing equations for multi-material flows along with the strategies for material modeling cast in a Cartesian grid-based Eulerian framework is presented in Sects. 7.2.1 and 7.2.2. Following that the numerical methods for solving the governing equations are discussed in Sect. 7.2.3. The interfacial treatment through the levelsets and GFM are described in Sects. 7.2.4, 7.2.5, and 7.2.6. Results obtained from several different multi-material flow problems are presented in Sect. 7.3. At the end, the concluding remarks and the scopes for future work are discussed in Sect. 7.4.

7.2   Methods

A Eulerian sharp-interface multiphase framework to perform reactive mesoscale simulations involving different phases, i.e., solid, liquid, or gas under shock loading is presented. A detailed description of the governing equations, constitutive models and numerical algorithms are discussed in this section.

7.2.1   Governing Equation

The governing equations for compressible multiphase systems are solved in the following form:

$$\frac{\partial}{\partial t}(\rho Y_k) + \frac{\partial}{\partial x_j}(\rho u_j Y_k) = \frac{\partial}{\partial x_j}(-J_{j,k}) + \dot{\omega_k} \qquad (7.1)$$

$$\frac{\partial}{\partial t}(\rho u_i) + \frac{\partial}{\partial x_j}\left(\rho u_i u_j - \sigma_{ij}\right) = \mathrm{M}_i \tag{7.2}$$

$$\frac{\partial}{\partial t}(\rho E) + \frac{\partial}{\partial x_j}\left[u_j\left(\rho E - \sigma_{ij}\right)\right] = \frac{\partial}{\partial x_j}\left(-q_j\right) + S_E \tag{7.3}$$

where ρ, u_i, σ_{ij}, q_j, and E are the density, velocity components, Cauchy stress tensor, heat flux, and the specific total energy (kinetic and internal), respectively. The subscript k is an index for identifying species in the multicomponent system. Y_k, $J_{j,k}$, and $\dot{\omega}_k$ are the mass fraction, diffusion mass flux, and the rate of production or destruction of the mass of the kth species. The source terms M_i and S_E account for the exchange of momentum and energy between the different phases due to phase change at the sharp interface. The Cauchy stress tensor σ_{ij} is decomposed into the deviatoric τ_{ij} and dilatational part $p\delta_{ij}$ as,

$$\sigma_{ij} = -p\delta_{ij} + \tau_{ij} \tag{7.4}$$

The definition of the deviatoric τ_{ij} and dilatational part $p\delta_{ij}$ changes with the phase description. A detailed description of the constitutive models for different phases is presented next.

7.2.2 Constitutive Models

Constitutive models for Solids
For the compressible flow of deformable solid materials, the dilatational part of the stress, i.e., pressure in Eq. (7.4) is described using Mie–Gruneisen equation of state (Meyers 1994) form as:

$$p(e, V) = p_c(V) + \Gamma(V)\frac{(e - e_c(V))}{V} \tag{7.5}$$

where $V = 1/\rho$ is the specific volume, p_c is the cold curve, and e_c is the energy along the isotherm and Γ is the Gruneisen parameter. For metals which feature in the applications presented in the results section, such as nickel and aluminum, p_c is expressed as,

$$p_c(V) = \frac{\rho_0 c_0^2 \eta}{1 - s\eta^2} \tag{7.6}$$

where $\eta = 1 - \frac{V}{V_0}$, ρ_0 is the speed of sound, and s is the material parameter. The values for the material parameters used in the current analysis are provided in the

previous work (Sambasivan et al. 2013). The energy on the isotherm e_c is obtained as,

$$e_c(V) = e_0 - \int_{V_0}^{V} p_c(V)\mathrm{d}V \qquad (7.7)$$

where e_0 is the reference energy at 0 K (usually set to 0).

The deviatoric response of the solid materials (exhibiting elastoplastic behavior) τ_{ij} is modeled using a hypo-elastic formulation where the rate of deviatoric stress tensor $\dot{\tau}_{ij}$ is related to the rate of change of strain rate tensor D_{ij} which is expressed in terms of velocity components as,

$$D_{ij} = \frac{1}{2}\left(\frac{\partial u_i}{\partial x_j} + \frac{\partial u_j}{\partial x_i}\right) \qquad (7.8)$$

The response of elastoplastic materials to high intensity (shock/impact) loading conditions are modeled by assuming the additive decomposition:

$$D_{ij} = D_{ij}^e + D_{ij}^p \qquad (7.9)$$

where D_{ij}^e and D_{ij}^p are the elastic and plastic strain rate components, respectively, u_i and u_j are the velocity components. Assuming isochoric plastic flow ($\mathrm{tr}(D_{ij}^p) = 0$), the volumetric or dilatational response is governed by an equation of state (Eq. 7.5) while the deviatoric response follows the conventional theory of plasticity. Using Eq. (7.10), the rate of change of deviatoric stress component can be modeled using a hypo-elastic stress-strain relation:

$$\hat{\tau}_{ij} = 2G\left(\overline{D}_{ij} - D_{ij}^p\right) \qquad (7.10)$$

where G is the modulus of rigidity, $\hat{\tau}_{ij}$ is the Jaumann derivative, and $\overline{D}_{ij}$ is the deviatoric strain rate component.

The Jaumann derivative is used to ensure the objectivity of the stress tensor with respect to rotation and expressed as,

$$\hat{\tau}_{ij} = \dot{\tau}_{ij} + \tau_{ik}\Omega_{kj} - \Omega_{ik}\tau_{kj} \qquad (7.11)$$

where Ω_{ij} is the spin tensor:

$$\Omega_{ij} = \frac{1}{2}\left(\frac{\partial u_i}{\partial x_j} - \frac{\partial u_j}{\partial x_i}\right) \qquad (7.12)$$

The deviatoric strain rate component in Eq. (7.10) is given by:

$$\overline{D}_{ij} = D_{ij} - \frac{1}{3} D_{kk} \delta_{ij} \tag{7.13}$$

The isochoric plastic strain rate component $\left(D_{ij}^p = \overline{D}_{ij}^p \right)$ in Eq. (7.10) is modeled assuming a coaxial flow theory (Drucker's postulate) for strain hardening material (Khan and Huang 1995):

$$D_{ij}^p = \Lambda N_{ij} \tag{7.14}$$

where $N_{ij} = \tau_{ij} / \sqrt{\tau_{kl} \tau_{kl}}$ is the outward normal to the yield surface and Λ is a positive scalar factor called the consistency parameter (Ponthot 2002).

To update the stress state of the elastoplastic solid materials, first, an elastic predictor step is performed by solving the stress equation,

$$\frac{\partial}{\partial t} \left(\rho \tau_{ij} \right) + \frac{\partial}{\partial x_j} \left(u_j \tau_{ij} \right) = 2G \left(\overline{D}_{ij} \right) + \Omega_{ik} \tau_{kj} - \tau_{ik} \Omega_{kj} \tag{7.15}$$

along with the conservation of mass, momentum, and energy equations (Eqs. 7.1–7.3). After the elastic update, the plastic deformation of the material is incorporated using the radial return algorithm given by Ponthot (2002), where the elastic stress is brought back to the yield surface. The Johnson–Cook model defined the yield surface as,

$$\sigma_Y = \left[A + B \left(\bar{\varepsilon}^p \right)^n \right] \left[1 + C \ln \left(\frac{\dot{\bar{\varepsilon}}^p}{\dot{\bar{\varepsilon}}^p} \right) \right] \left[1 - \theta^m \right] \tag{7.16}$$

where σ_Y is the yield stress, $\bar{\varepsilon}^p$ is the effective plastic strain, $\dot{\bar{\varepsilon}}^p$ is the effective plastic strain rate, A, B, C, n, m, and $\dot{\varepsilon}_0^p$ are the model constants and $\theta = \frac{T - T_0}{T_m - T_0}$ (T is the temperature, T_0 and T_m are the reference and melting temperature).

The details regarding the calculation of $\bar{\varepsilon}^p$ and $\dot{\bar{\varepsilon}}^p$ from the radial return algorithm is presented in the previous work (Sambasivan et al. 2013). The temperature T is calculated as,

$$T = T_0 + \frac{e - e_0}{C_V} \tag{7.17}$$

where e is the specific internal energy obtained from the energy equation (Eq. 7.3), e_0 is the reference energy, and C_V is the specific heat at constant volume for the solid material.

Constitutive models—for Liquids and Gas
For the liquid and gaseous phase, the dilatational part, i.e., pressure in Eq. (7.4) is obtained based on the different equation of state models available in the literature. Tait equation of state [ref] is used for water and liquid aluminum. Air and vapor are modeled using the ideal gas equation of state. The JWL equation of state (Massoni

Table 7.1 Initial conditions for the simulation of shock-induced combustion of an aluminum droplet

	ρ (kg/m^3)	P (Pa)	u (m/s)	T (K)
Pre-shocked air ($x \geq 8.64$ m)	1.2	101,325.0	0.0	291.5
Post-shocked air ($x < 8.64$ m)	5.13	1431,216.0	225.91	966.5
Droplet	2030.0	181,582.8	0.0	2743.0

et al. 1999) is used for the gaseous mixture formed after decomposition of energetic materials such as HMX. The expressions for the different equation of states are briefly discussed below.

Tait equation of state for liquids:
The Tait EOS in the following form is used to obtain p in the liquid phase:

$$p = B \left[\left(\frac{\rho}{\rho_0} \right)^N - 1 \right] + A \qquad (7.18)$$

where A, B, N, and ρ_0 are physical constants and depend on the material (Liu et al. 2005; Houim and Kuo 2013). The values of physical constants used in this work for water and liquid aluminum are shown in Table 7.1.

JWL equation of state for reaction products for HMX:
The JWL equation of state is used for the reaction products obtained from the decomposition of solid HMX:

$$p = A \left[1 - \frac{\omega V_0}{V R_1} \right] \exp(-R_1 V / V_0) + B \left[1 - \frac{\omega V_0}{V R_2} \right] \exp(-R_2 V / V_0) \qquad (7.19)$$

where $V = 1/\rho$ is the specific volume, ω is the Gruneisen parameter, and A, B, R_1, and R_2 are material parameters obtained from the work of Massoni et al. (1999).

For the liquid phase, the deviatoric or the viscous stress tensor in Eq. (7.4) is given by:

$$\tau_{ij} = \mu \left(\frac{\partial u_i}{\partial x_j} + \frac{\partial u_j}{\partial x_i} \right) - \frac{2}{3} \mu \frac{\partial u_j}{\partial x_j} \delta_{ij} \qquad (7.20)$$

where μ is the viscosity of the liquid.

It is important to note that for the liquid and gas phases, the stress update equation is not solved (unlike solids) and the deviatoric stress is obtained after solving the mass, momentum, and the energy equations (Eqs. 7.1–7.3).

Constitutive models—Thermal and Species Diffusion
The heat fluxes due to thermal diffusion and species diffusion effects are obtained from:

$$q_j = \sum_{k=1}^{N} J_{j,k} h_k - \frac{\partial(kT)}{\partial x_j} \tag{7.21}$$

where N is the total number of species in the gaseous phase. h_k is the specific enthalpy of kth, μ and k are the mixture averaged viscosity and thermal conductivity.

The diffusion mass flux $(J_{j,k})$ of the kth species is obtained from:

$$J_{j,k} = \rho Y_k v_{j,k} \tag{7.22}$$

where $v_{j,k}$ is the diffusion velocity of the kth species along the jth direction. The diffusion velocities are first calculated from:

$$\widehat{v_{j,k}} = -\frac{D_{k,\text{mix}}}{X_k}\left(\frac{\partial X_k}{\partial x_j} + (X_k - Y_k)\frac{\partial(\ln p)}{\partial x_j}\right) \tag{7.23}$$

where X_k is the mole fraction of the kth species. The mixture averaged diffusion coefficient $D_{k,\text{mix}}$ is obtained from binary diffusion coefficients D_{kl} using:

$$D_{k,\text{mix}} = \frac{1 - Y_k}{\sum_{l=1,k\neq l}^{N} X_l/D_{kl}} \tag{7.24}$$

The diffusion velocities of the kth species are then corrected to ensure mass conservation (Powell et al. 2001):

$$v_{j,k} = \widehat{v_{j,k}} - \sum_{k=1}^{N} Y_k \widehat{v_{j,k}} \tag{7.25}$$

The source term in the species transport Eq. (7.1), $\dot{\omega}_k$ accounts for the vapor added to the gaseous phase at the interface and the change in species concentration:

$$\dot{\omega}_k = \dot{\omega}_{k,\text{evap}} + \dot{\omega}_{k,\text{react}} \tag{7.26}$$

$\dot{\omega}_{k,\text{evap}}$ accounts the change in vapor mass fraction at the grid points near the droplet surface due to evaporation and $\dot{\omega}_{k,\text{react}}$ accounts for the change in the mass fraction of all the species involved in the chemical reaction.

$\dot{\omega}_{k,\text{evap}}$ is computed from the following equation:

$$\dot{\omega}_{k,\text{evap}} = \begin{cases} 0, & \text{for } k = 1 \\ \frac{\dot{m}'' A_{\text{int}}}{V}, & \text{for } k = 2 \end{cases} \tag{7.27}$$

where A_{int} is the area of the interface within a computational cell. V is the volume occupied by the gaseous phase in a cell. A_{int} and V are computed using algorithms described in Mousel (2012), Scardovelli and Zaleski (2000). $\dot{m}''$ is the evaporation

mass flux at the gas–liquid interface and is computed from the Scharge-Knudsen equation (Houim and Kuo 2013):

$$\dot{m}'' = \frac{2C}{2-C}\sqrt{\frac{\mathrm{Mw}_k}{2\pi R_u}}\left(\frac{P_{\mathrm{sat}}}{\sqrt{T_l}} - \frac{P_v}{\sqrt{T_g}}\right) \qquad (7.28)$$

where

$$C = \left\{1 - \left(\frac{\rho_g}{\rho_l}\right)^{\frac{1}{3}}\right\}\exp\left(-\frac{1}{2\left(\rho_l/\rho_g\right)^{1/3} - 2}\right)$$

where R_u is the universal gas constant and Mw_k is the molecular weight of the kth species.

For problems involving shock-induced chemical reactions, the source term $\dot{\omega}_{k,\mathrm{react}}$ in Eq. (7.26) is obtained using the Arrhenius-based chemical kinetic model. For instance, energetic materials such as HMX can undergo decomposition depending on the temperature rise. To model the chemical decomposition of HMX, a three steps Arrhenius model given by Tarver et al. (1996) defines the $\dot{\omega}_{k,\mathrm{react}}$. Gas-phase combustion of aluminum vapor in the air is modeled using a 11 equation reaction model (Huang et al. 2009).

The source terms M_i represent the momentum exchange between the gas and the liquid phase due to the phase change at the interface. M_i is calculated from:

$$M_i = \frac{\dot{m}'' A_{\mathrm{int}}}{V} u_i \qquad (7.29)$$

The source term in the energy equation, S_E, represents the total energy associated with the phase changes and is calculated from:

$$S_E = \sum_{k=1}^{N} \frac{\dot{m}'' A_{\mathrm{int}}}{V}\left[\left(h_{f,k} + \int_{T^o}^{T} C_{p,k}(\tau)\mathrm{d}\tau\right) - \frac{R_u}{\mathrm{Mw}_k}T\right] \qquad (7.30)$$

where $h_{f,k}$ is the specific enthalpy of formation of the kth species at the reference state ($T^0 = 298$ K). $C_p^k(T)$ is the specific heat capacity at a constant pressure of the kth species, at a temperature T. $C_{p,k}(T)$ is a polynomial function of temperature T in the absolute scale and taken from (Burcat's Thermodynamic Data).

In the problems involving chemical reactions or phase changes, each of the Eulerian computation grid cells defines the mixture average pressure of the grid point, i.e.:

$$p = \sum_{k=1}^{n} p_k \qquad (7.31)$$

where p_k is the partial pressure of the kth component of the gaseous mixture.

The average temperature (T) of the mixture is obtained by solving the following equation for total specific energy (E) of the system using the Newton-Raphson method:

$$E(T) = \sum_{k=1}^{n} \left[Y_k \left(h_{f,k} + \int_{T^o}^{T} C_{p,k}(\tau)d\tau \right) - \frac{R_u}{\mathrm{Mw}_k} T \right] + \frac{u^2 + v^2 + w^2}{2} \quad (7.32)$$

7.2.3 Numerical Schemes

The numerical schemes to solve the system of equations described in Sects. 7.2.1 and 7.2.2 are briefly discussed in this section. Since there are different timescales involved in the governing equations for convection, thermal, and species diffusion and reaction, the numerical scheme for the governing equations is based on an operator splitting algorithm. The splitting of the operators is decided based on the relative timescales of the physical process which can be determined *a priori* using the material parameters relevant for the physical processes. For instance, the species, momentum and thermal diffusion coefficients can inform about the relative time scales. Depending on the operators, the numerical schemes can vary.

The hyperbolic terms in the governing equations are first integrated using a third-order Runge–Kutta (TVD-RK) (Gottlieb and Shu 1998) scheme to obtain an intermediate solution state U^* at the nth timestep:

$$U^* = H^{\Delta t}(\mathbf{U}^n) \quad (7.33)$$

where U^n is the solution state at the end of the nth timestep. $H^{\Delta t}()$ is the linearized operator for integrating the hyperbolic terms in the governing equations. The parabolic terms in the governing equations are integrated using the Runge–Kutta–Chebyshev (RKC) explicit time integration scheme (Verwer et al. 2004) to obtain a second intermediate state U^{**} from U^*:

$$U^{**} = P^{\Delta t}(\mathbf{U}^*) \quad (7.34)$$

where $P^{\Delta t}()$ is the operator for integrating the parabolic terms.

Finally, the source terms are integrated using a fifth-order explicit Runge–Kutta–Fehlberg scheme to obtain the solution at the $n + 1$th timestep:

$$U^{n+1} = S^{\Delta t}(\mathbf{U}^{**}) \quad (7.35)$$

The timestep size Δt is from the CFL number:

$$\Delta t = \text{CFL} \left[\frac{\Delta x}{u + a} \right]_{\min} , \text{ where CFL} \leq 1 \text{ and a is the wave speed} \qquad (7.36)$$

A third-order accurate ENO-LLF (Shu and Osher 1989) scheme is used for spatial discretization of the hyperbolic terms in the governing equations. A fourth-order accurate finite difference scheme (Das 2017) is used to discretize the parabolic terms.

7.2.4 Interface Tracking Using Levelsets

The levelset method (Osher and Sethian 1988; Sethian and Smereka 2003) is used in this work to define the interface between the gaseous and the liquid phases. The zero-levelset contour defines the location of the sharp interface between the liquid and the gaseous phases. A narrow-band levelset field provides the signed normal distance to the nominal interface from any point in a band around the sharp interface. The levelset field is advected to capture the evolution of the interface as the flow evolves in time:

$$\frac{\partial \phi}{\partial t} + \mathbf{u_n} \cdot \nabla \phi = 0 \qquad (7.37)$$

where ϕ represents the levelset field. $\mathbf{u_n}$ is the normal velocity of the interface. The levelset field is advected at the end of each flow timestep to capture the evolution of the gas–liquid interface. The third-order TVD-Runge–Kutta method is used to perform the time integration. The fifth-order WENO scheme (Jiang and Shu 1996) is used for spacial discretization of Eq. (7.37). The high-order discretization scheme maintains the accuracy of the levelset advection and mitigates the mass-conservation error caused by numerical diffusion. The levelset field is reinitialized (Sussman et al. 1994) every five timesteps to ensure that it remains a signed distance function. The different materials separated by the zero-levelset contours are coupled using a modified ghost fluid method (GFM), which is described next.

7.2.5 Boundary Conditions at the Interface

The flow calculations in the different materials or phases separated by the sharp interfaces are coupled through the appropriate boundary conditions. The boundary conditions or the interfacial jump conditions depend on the materials separated by the interface. The appropriate boundary conditions for different types of interfaces are described in the following sub-sections.

Boundary treatment of solid–solid interfaces:
In problems where deformable solids interact with each other on parts of the interface, continuity of normal stress components and the continuity of normal velocity

components are enforced. No constraint is applied to the tangential components of stress and velocity fields.

The velocity field and stress states are transformed in the local normal and tangential directions at each grid points as,

$$u_n = |\vec{u}_n| = \vec{u}.\hat{n} \tag{7.38}$$

$$u_s = |\vec{u}_s| = \vec{u}.\hat{s} \tag{7.39}$$

where $\vec{u}$ is the velocity vector in the Cartesian coordinates, $\vec{u}_n$ and $\vec{u}_s$ are the normal and tangential velocity vectors.

The total stress tensor in the normal and tangential coordinates is given by

$$\tilde{\sigma} = J\sigma J^T \tag{7.40}$$

where $J = \begin{pmatrix} n_x & n_y \\ s_x & s_y \end{pmatrix}$ is the Jacobian matrix and $\hat{n}$ and $\hat{s}$ are local normal and tangential vectors defined at the interface.

The coupling of the normal component of stress and velocity and decoupling of the tangential components ensures frictionless sliding between the materials. Thus, at the interfaces:

$$\left[\vec{u}.\hat{n}\right] = 0 \tag{7.41}$$

$$[\tilde{\sigma}_{nn}] = 0 \tag{7.42}$$

$$[\tilde{\sigma}_{ns}] = 0 \tag{7.43}$$

$$[P] = 0 \tag{7.44}$$

where $\tilde{\sigma}_{nn}$ and $\tilde{\sigma}_{ns}$ are the normal components of the stress tensor, P is pressure, and $\vec{u}$ is the velocity vector.

Boundary treatment of solid–void interfaces:
This type of interfacial condition arises whenever the deformable solid interface interacts with a surrounding void, i.e., at a free surface. Conditions corresponding to physically consistent wave reflection phenomena are enforced at all free surfaces. Therefore, zero-traction conditions on the normal stress components are enforced on those portions of the interface that are free surfaces, viz.:

$$\tilde{\sigma}_{nn} = 0 \tag{7.45}$$

$$\tilde{\sigma}_{ns} = 0 \tag{7.46}$$

Boundary treatment of fluid–rigid solid interfaces:

Interfaces between fluid and rigid solids are encountered in the simulations of particle-laden flows. In such calculations, the particles are assumed as rigid solids, i.e., particle deformation is neglected, and a no-slip and no-penetration boundary conditions are enforced at the fluid–rigid solid interfaces. A Dirichlet boundary condition is applied for the velocity components in the fluid. The velocity of the fluid at the interface is set to the velocity of the solid–fluid interface representing the embedded rigid object (u_I).

For pressure and density, Neumann boundary conditions are enforced at the solid–fluid interface. The density boundary condition is as follows:

$$\frac{\partial \rho}{\partial n} = 0 \tag{7.47}$$

A normal force balance at the interface provides the pressure boundary condition:

$$\frac{\partial p}{\partial n} = \frac{\rho_s u_{I,t}^2}{R} - \rho_s a_n \tag{7.48}$$

where $u_{I,t}$ is the magnitude of the tangential component of velocity of the fluid at the interface and a_n is the magnitude of the normal component of acceleration of the solid–fluid interface (a_Γ).

Boundary treatment of fluid-fluid interfaces:

Fluid–fluid interfaces are encountered in problems involving bubbles or droplets suspended in a gas. The interactions of the gas and liquid at the interface are further complicated by the effects of surface tension and phase change. The interaction of the two fluids at the interface is described by the following jump conditions:

$$[u_n] = \dot{m}'' \left[\frac{1}{\rho} \right] \tag{7.49}$$

$$[p] = -\gamma \kappa - \dot{m}''[u_n] - [\tau_{nn}] \tag{7.50}$$

$$[\tau_{ns}] = -\frac{d\gamma}{ds} \tag{7.51}$$

$$[\dot{q}''_{\mathrm{cond}}] = -\dot{m}''[h] + [\tau_{nn} u_n] + [\tau_{ns} u_s] \tag{7.52}$$

where the operator [ ] represents:

$$[\chi] = \chi_g - \chi_l$$

χ is any flow variable of interest. The subscripts g and l represent the flow variables at the interface in the gaseous and the liquid phase, respectively. The subscripts n and s represent the directions normal and tangential to the interface. γ is the local

surface tension at the gas–liquid interface. κ is the local curvature at the interface and is calculated from the levelset field (Sussman et al. 1994).

Equation (7.49) accounts for the jump in the normal velocity of the two phases at the interface caused by vaporization or condensation. Equation (7.50) describes the jump in pressure at the interface due to surface tension ($-\gamma\kappa$), vaporization ($\dot{m}[u_n]$), and jump in the normal component of viscous stress (τ_{nn}). The jump in the tangential components of the deviatoric stress tensor ($[\tau_{ns}]$) in Eq. (7.51) represents the effect of Marangoni stresses at the interface. The jump in the heat flux ($\left[\dot{q}''_{\text{cond}}\right]$) is given by Eq. (7.52). It accounts for the latent heat of evaporation ($\dot{m}[h]$) and the work done by the viscous stresses ($[\sigma_{nn}u_n]$, $[\sigma_{ns}u_s]$).

The above-mentioned jump conditions for the different types of interfaces are implemented through the ghost fluid method to couple the flow fields of different materials at the sharp interface. The implementation of the GFM for these different types of boundary conditions is described in the following section.

7.2.6 *The Ghost Fluid Method*

The ghost fluid method is used to supply appropriate boundary conditions at the sharp interface. The ghost fluid method was originally proposed by Fedkiw et al. (1999). In GFM, extra few layers of computational cells, defined as ghost layers, are added beyond the sharp-interface boundary for each phase. Figure 7.1 shows a schematic of a computational grid with an embedded interface to demonstrate the categorization of the computational points into the "bulk points" in the material and the "ghost points" within the ghost layer around the interface. The number of ghost layers depends on the stencil size and order of the discretization scheme. The ghost points provide the boundary conditions for the flow calculations at the computational cells of their corresponding phase near the interface. The "ghost layer" is populated such that the appropriate boundary condition at the sharp interface is imposed. There are two steps in populating the ghost points with the ghost values. In the first step, first, the flow field near the interface is reconstructed from the data available at the bulk points in the vicinity of the interface to estimate the flow variables near the interface. In the second step, the flow variables near the interface obtained from the reconstructed flow field are used to estimate the ghost value for any flow variables at the ghost point such that the boundary condition/interfacial jump condition for that variable at the interface is satisfied.

Estimation of the flow variables near the interface:
Flow variables near the interface are estimated to extend the flow field from the bulk points to the ghost points. However, in the Cartesian grid-based sharp-interface methods, the grid points often do not align with the location of the interface. Therefore, to obtain the values of the flow variables near the interface, the flow field is reconstructed along the interface normal direction.
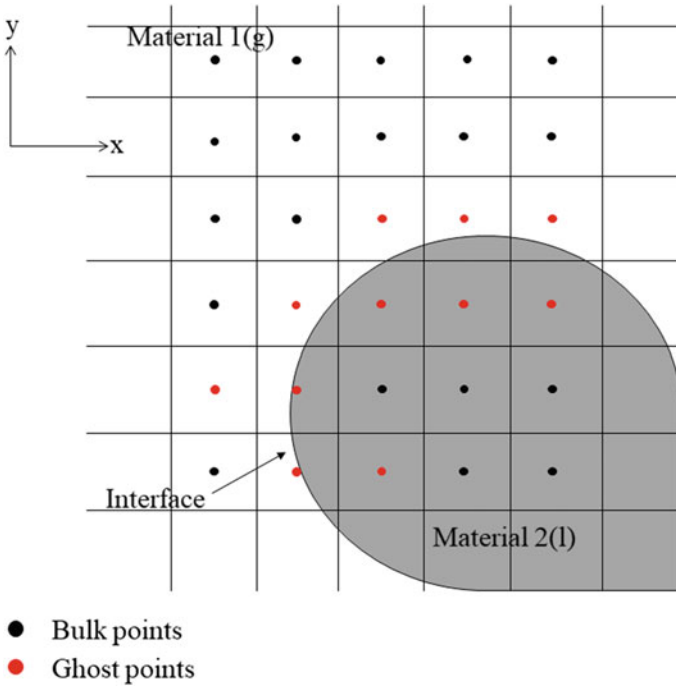
**Fig. 7.1**   Categorization of the computational cells

The numerical methods for obtaining the flow variables near the interface in the current levelset-based framework is explained through the following example of a typical ghost point with respect to material 1 IG in Fig. 7.2. The flow variables near the interface are obtained by probing the material 1 at a distance $1.5\Delta x$ from the interface in the gaseous phase. To probe for values of the field variables, first, the normal projection of IG on the interface, (point labeled I in Fig. 7.2) is obtained. The location of I is obtained from the following equation:

$$\mathbf{X}_I = \mathbf{X}_{IG} - \phi_{IG} * \mathbf{n}_{IG} \tag{7.53}$$

where ϕ_{IG} is the magnitude of the levelset field at the point G and $\mathbf{n}_{IG}$ is the unit vector normal to the interface computed at G from the levelset field (Sussman et al. 1998). X_I and $\mathbf{X}_{IG}$ are the locations of the points I and IG, respectively. Following this, a probe is inserted in the material 1. The probe is $1.5\Delta x$ away from the point I on the interface. The location of the probe is given by the following equations:

$$\mathbf{X}_F = \mathbf{X}_I + 1.5\Delta x * \mathbf{n}_{IG} \tag{7.54}$$

where $\mathbf{X}_F$ is the position of the endpoint of the probe F. A convex hull is formed around F using neighboring grid points in the vicinity, as shown in Fig. 7.2. The
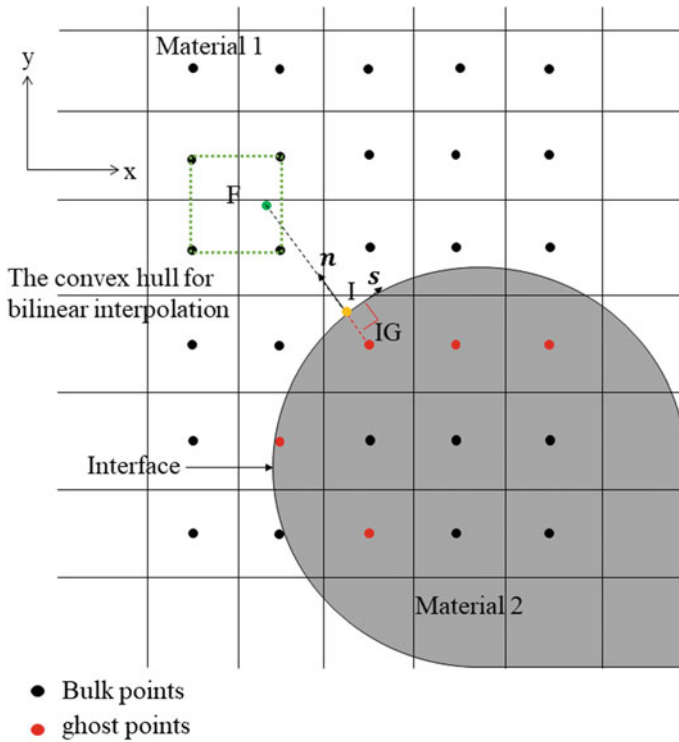
Fig. 7.2 Numerical method for reconstructing the flow field near the interface

flow variables, e.g., pressure (p_F), density (ρ_F), and velocity ($\boldsymbol{u}_F$) at F are obtained using bilinear interpolation from values at the grid points forming the convex hull. The field variables at F interpolated from the computational grid are extended to the ghost point IG while imposing appropriate boundary conditions at the interface.

Calculation of the ghost values from the flow variables estimated near the interface
The ghost values of the flow variables at the ghost points are calculated from the reconstructed flow field near the interface. The ghost values are computed such that the appropriate boundary conditions/interfacial jump conditions are satisfied. The boundary conditions depend on the type of interface. The numerical method for implementing the appropriate boundary conditions for solid–solid, solid–void, fluid–rigid solid, fluid–fluid, and solid–solid interfaces are described in the following sub-sections.

Solid– solid interface
The interaction between two deformable solids is modeled by populating ghost values that satisfy the continuity of normal velocity, pressure, and normal component of the stress tensor as described in Sect. 7.2.5. The ghost point for material 1 in material 2, i.e., the point IG, is populated with the following conditions for the field variables,

The density field is supplied using a zero gradient, i.e., Neumann condition:

$$\rho_{IG} = \rho_F \tag{7.55}$$

The continuity of pressure is enforced at the ghost node IG in material 2 by simply injecting the node with the real value of the pressure in material 2 as,

$$p_{IG} = p_{IG}^{\text{real}} \tag{7.56}$$

Similar to the pressure, the continuity of normal velocity is applied by initializing the normal component of the velocity vector with the real value (from material 2) of the normal velocity component at node IG:

$$u_{n,IG} = u_{n,IG}^{\text{real}} \tag{7.57}$$

The tangential velocity component at IG is extended using the zero-gradient condition,

$$u_{s,IG} = u_{t,F} \tag{7.58}$$

The stress tensor at the ghost node IG is reconstructed by enforcing the zero-gradient condition for the tangential components and continuity of normal stress components,

$$\widetilde{\sigma}_{IG} = \begin{pmatrix} \widetilde{\sigma}_{ns}^{\text{real}} & \widetilde{\sigma}_{ns}^{\text{real}} \\ \widetilde{\sigma}_{ns}^{\text{real}} & \widetilde{\sigma}_{ss,F} \end{pmatrix} \tag{7.59}$$

Solid–void interface:
For the solid–void interface, conditions corresponding to the physically correct wave reflections are enforced. For instance, at the free surface, a compressive wave is reflected back as a tensile wave and vice versa. Therefore, zero-traction conditions for the normal stress components are enforced. The other field variables, i.e., density and velocity components are initialized with the zero-gradient conditions.

The field variables at the ghost node, IG for the solid–void interface is populated as,

$$\rho_{IG} = \rho_F \tag{7.60}$$

$$u_{n,IG} = u_{n,F} \tag{7.61}$$

$$u_{s,IG} = u_{s,F} \tag{7.62}$$

$$p_{IG} = p_F \tag{7.63}$$

The zero-traction conditions, i.e., zero value of the normal stress components at the interface are applied at the ghost node *IG*,

$$\widetilde{\sigma}_{IG} = \begin{pmatrix} -\widetilde{\sigma}_{nn,F} & -\widetilde{\sigma}_{nn,F} \\ -\widetilde{\sigma}_{nn,F} & \widetilde{\sigma}_{ss,F} \end{pmatrix} \tag{7.64}$$

Fluid–rigid solid interface:
The no-slip boundary condition is applied at the fluid–rigid solid interface. The ghost values for the flow variables at a typical ghost point *IG* (Fig. 7.2) for a fluid–rigid solid interface are described in this section. A Neumann boundary condition for the pressure and density are imposed at the interface by setting

$$p_{IG} = p_F \tag{7.65}$$

and

$$\rho_{IG} = \rho_F \tag{7.66}$$

where ρ_{IG} and ρ_{IG} are the ghost values of pressure and density at the ghost point *IG*. A no-slip boundary conditions for velocity is used. For that $\boldsymbol{u}_F$ is first decomposed into the components normal and tangent to the interface, as given below:

$$\begin{pmatrix} u_{n,F} \\ u_{s,F} \end{pmatrix} = \begin{bmatrix} n_x & n_y \\ n_y & -n_x \end{bmatrix} \begin{pmatrix} u \\ v \end{pmatrix} \tag{7.67}$$

where $u_{n,F}$ and $u_{s,F}$ are the components of $\boldsymbol{u}_F$ along the normal and the tangential direction of the interface. u and v are the components of $\boldsymbol{u}_F$ along the x- and y-axis, respectively. n_x and n_y are the x and y components of $\boldsymbol{n}_{IG}$, respectively. The ghost values of the velocity components at *IG* $(u_{n,IG}, u_{s,IG})$ are calculated from the velocity of the gaseous phase and the velocity of the solid–gas interface using linear interpolation, as follows:

$$u_{n,IG} = \frac{u_{n,I}(\phi_{IG} + 1.5\Delta x) - \phi_{IG}u_{n,F}}{1.5\Delta x} \tag{7.68}$$

$$u_{s,IG} = \frac{u_{s,I}(\phi_{IG} + 1.5\Delta x) - \phi_{IG}u_{s,F}}{1.5\Delta x} \tag{7.69}$$

where $u_{n,I}$ and $u_{s,I}$ are the components of velocity of the interface along the normal and the tangential direction of the interface.

GFM treatment of the fluid–fluid interface:
Ghost values for the fluid–fluid interfaces are obtained such that Eqs. (7.49)–(7.52) are satisfied. However, only satisfying Eqs. (7.49)–(7.52) while computing the ghost values is not sufficient to ensure the coupling of the two phases at the interfaces. Equations (7.49)–(7.52) are coupled with a local 1D Riemann problem at the interface to

allow the characteristics waves in the bulk material to travel across the interfaces. However, solving Eqs. (7.49), (7.50), and (7.51) simultaneously in conjunction with an interfacial Riemann problem is computationally expensive. To avoid this problem, the interfacial jump conditions are decoupled and solved separately during the hyperbolic step and the parabolic step within an overall single flow timestep. The following 1D local Riemann problem along with the following interfacial jump conditions are solved to populate the ghost points before integrating the hyperbolic terms in the governing equations:

$$[u_n] = \dot{m}'' \left[\frac{1}{\rho} \right] \tag{7.70}$$

$$[p] = -\gamma \kappa - \dot{m}''[u_n] \tag{7.71}$$

The contributions from the parabolic terms for the two phases at the interface are coupled by populating the ghost points such that the following interfacial jump conditions are imposed at the interface:

$$[\tau_{nn}] = 0 \tag{7.72}$$

$$[\tau_{ns}] = -\frac{d\gamma}{ds} \tag{7.73}$$

$$\left[\dot{q}''_{cond} \right] = -\dot{m}''[h] + [\tau_{nn} u_n] + [\tau_{ns} u_s] \tag{7.74}$$

The methods adopted to obtain the ghost values for the hyperbolic and the parabolic steps are described in the following two sub-sections.

Treatment of interface for hyperbolic terms
An interfacial Riemann problem is solved to obtain p, ρ and u_n at the interfacial ghost points. Figure 7.3 shows a schematic to illustrate the numerical method for constructing a local 1D Riemann problem at a typical interfacial ghost point labeled *IG*. A local Riemann problem normal to the interface is constructed at the ghost point *G*. The initial conditions for the local Riemann problem are obtained from the flow variables (ρ, u_n, p) in the gaseous $(\rho_g, u_{n,g}, p_g)$ and the liquid $(\rho_l, u_{n,l}, p_l)$ phases near the interface.

A 1D Riemann problem is solved to obtain the intermediate (*) states from the flow variables in the gaseous phase $(\rho_g, u_{n,g}, p_g)$ and the liquid phase $(\rho_l, u_{n,l}, p_l)$ at the interface. The intermediate (*) states are used as the ghost values at the ghost points for each phase. In this formulation, the jumps in pressure and normal velocity of the intermediate (*) states across the contact discontinuity given by the following equations:

$$[u_n^*] = u_{n,g}^* - u_{n,l}^* = \dot{m}'' \left[\frac{1}{\rho} \right] \tag{7.75}$$
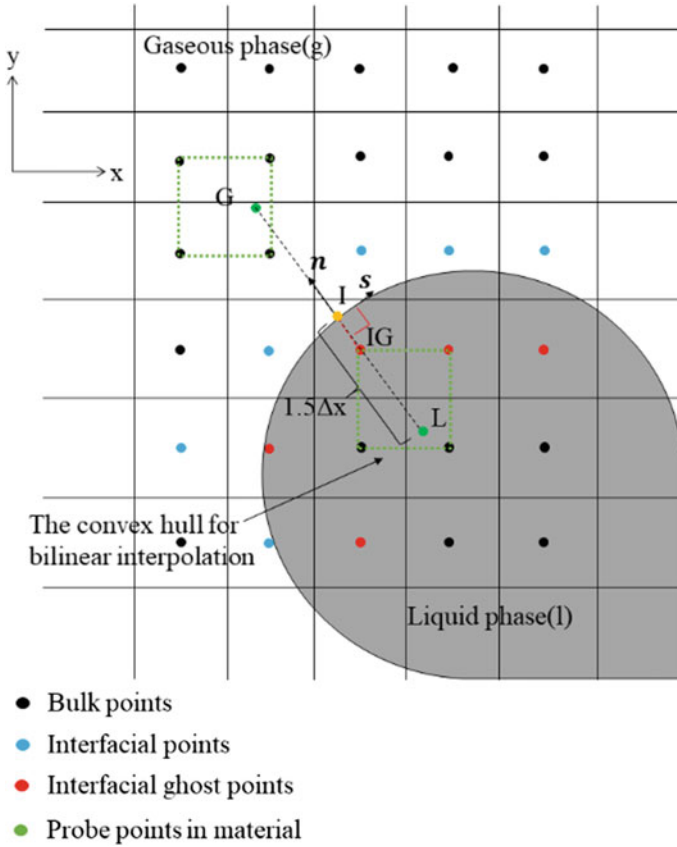
Fig. 7.3 Schematic for computing the ghost values during the hyperbolic step of the multi-step integration process

$$[p^*] = p_g^* - p_l^* = -\gamma\kappa - \dot{m}''[u_n] \tag{7.76}$$

are incorporated in the 1D Riemann problem. The Riemann problem takes the following algebraic form:

$$f_l\left(p_l^*, p_l, \rho_l, u_{n,l}\right) + f_g\left(p_g^*, p_g, \rho_g, u_{n,g}\right) + u_{n,g} - u_{n,l} + [u_n] = 0 \tag{7.77}$$

where

$$
f_g =
\begin{cases}
\left(p_g^* - p_g\right)\sqrt{\dfrac{A_g}{p_g^* - B_g}}, & \text{when } p_g^* > p_g \\
\dfrac{2a_g}{\gamma - 1}\left[\left(\dfrac{p_g^*}{p_g}\right)^{\frac{\gamma-1}{2\gamma}} - 1\right], & \text{when } p_g^* < p_g
\end{cases}
$$

$$A_g = \frac{2}{(\gamma + 1)\rho_g}$$

$$B_g = \frac{\gamma - 1}{\gamma + 1}(P_g + B)$$

$$a_g = \sqrt{\frac{\gamma P_g}{\rho_g}}$$

and

$$f_l = \begin{cases} (p_l^* - p_l)\sqrt{\dfrac{A_l}{(p_l^* + \overline{B}) - B_l}}, & \text{when } p_l^* > p_l \\[2ex] \dfrac{2a_l}{N-1}\left[\left(\dfrac{p_l^* + \overline{B}}{p_l + \overline{B}}\right)^{\frac{N-1}{2N}} - 1\right], & \text{when } p_l^* < p_l \end{cases}$$

$$A_l = \frac{2}{(N + 1)\rho_l}$$

$$B_l = \frac{N - 1}{N + 1}\left(p_l + \overline{B}\right)$$

$$a_l = \sqrt{\frac{N * \left(p_l + \overline{B}\right)}{\rho_l}}$$

$$\overline{B} = B - A$$

The Newton-Raphson method is used to solve Eq. (7.77). ρ_g^*, ρ_l^*, $u_{n,g}^*$, and $u_{n,l}^*$ are obtained from the following equations:

$$\rho_g^* = \begin{cases} \rho_g \sqrt{\dfrac{\frac{p_g^*}{p_g} + \frac{\gamma - 1}{\gamma + 1}}{\frac{\gamma - 1}{\gamma + 1}\frac{p_g^*}{p_g} + 1}}, & \text{when } p_g^* > p_g \\[2ex] \rho_g \left(\dfrac{p_g^*}{p_g}\right)^{\frac{1}{\gamma}}, & \text{when } p_g^* < p_g \end{cases} \tag{7.78}$$

$$\rho_l^* = \begin{cases} \rho_l \sqrt{\dfrac{\frac{p_l^* + \overline{B}}{p_l + \overline{B}} + \frac{N-1}{N+1}}{\frac{\gamma - 1}{\gamma + 1}\frac{p_l^* + \overline{B}}{p_l + \overline{B}} + 1}}, & \text{when } p_l^* > p_l \\[2ex] \rho_l \left(\dfrac{p_l^* + \overline{B}}{p_l + \overline{B}}\right)^{\frac{1}{N}}, & \text{when } p_l^* < p_l \end{cases} \tag{7.79}$$

$$u_g^* = \frac{u_g + u_l}{2} + \frac{f_g - f_l}{2} + \frac{\dot{m}''\left[\frac{1}{\rho}\right]}{2} \tag{7.80}$$

$$u_l^* = \frac{u_g + u_l}{2} + \frac{f_g - f_l}{2} - \frac{\dot{m}''\left[\frac{1}{\rho}\right]}{2} \tag{7.81}$$

ρ_g^*, $u_{n,g}^*$, and p_g^* are obtained by solving the 1D interfacial Riemann problem at I and are used as the ghost values for the gaseous phase. Similarly, ρ_l^*, $u_{n,l}^*$, and p_l^*, computed from the 1D interfacial Riemann problem are used as ghost values at the interfacial ghost points with respect to the fluid phase. These ghost values for density, velocity, and pressure at the interfacial ghost points are extrapolated to the interior ghost points using a PDE-based multidimensional extrapolation approach (Meyers 1994).

The GFM for the parabolic terms

The GFM treatment at the interface for the parabolic terms in the governing equations is different from the hyperbolic terms. The ghost values for velocity and temperature are calculated separately before integrating the parabolic terms in the governing equation such that Eqs. (7.72)–(7.74) are satisfied.

Calculation of the velocity field in the ghost fluid region

The numerical method for computing the ghost values of velocity components for coupling the parabolic terms at the interface is described in this section in the context of a typical ghost point *IG* in Fig. 7.3. The ghost values of the velocity at *IG* are obtained by solving Eqs. (7.72) and (7.73). which can be written in the following forms:

$$[\tau_{nn}] = \left[2\mu \frac{\partial u_n}{\partial n} - \frac{2}{3}\mu \left(\frac{\partial u_n}{\partial n} + \frac{\partial u_s}{\partial s} \right) \right] = 0 \tag{7.82}$$

$$[\tau_{ns}] = \left[\mu \left(\frac{\partial u_s}{\partial n} + \frac{\partial u_n}{\partial s} \right) \right] = -\frac{d\gamma}{ds} \tag{7.83}$$

where u_n and u_s are the components of velocities of the fluid phases along the normal and the tangential direction of the interface calculated using Eq. (7.67). The derivatives of u_n and u_s in Eqs. (7.82) and (7.83) can be approximated from the reconstructed velocity field of the corresponding phases around the interface. Now, the velocity of the two phases at the interface is not readily available because the Cartesian grid does not align with the interface. The velocity of the fluids at the interface can be obtained solving Eqs. (7.82) and (7.83) along with the jump conditions for the velocity field at the interface given by the following equations:

$$u_{n,I,g} - u_{n,I,l} = [u_{n,I}] = \dot{m}'' \left[\frac{1}{\rho} \right] \tag{7.84}$$

$$u_{s,I,g} - u_{s,I,l} = [u_{s,I}] \tag{7.85}$$

where $u_{n,I}$ and $u_{s,I}$ are the components $\boldsymbol{u}_I$ along the normal and the tangential direction of the interface. $u_{n,I,g}$ and $u_{s,I,g}$ are the velocity components of the gaseous phase along $\boldsymbol{n}$ and $\boldsymbol{s}$ at the point I in Fig. 7.3. $u_{n,I,l}$ and $u_{s,I,l}$ are the velocity components of the liquid phase along $\boldsymbol{n}$ and $\boldsymbol{s}$ at the point I.

The ghost values of the velocity at IG $\left(\boldsymbol{u}_{IG}|_{\text{ghost}} \right)$ are extrapolated from the velocity of the gaseous phase at the interface $\left(\boldsymbol{u}_{I,g} \right)$ and the point G $(\boldsymbol{u}_G)$, so that:

$$\boldsymbol{u}_{IG}|_{\text{ghost}} = \frac{\boldsymbol{u}_{I,g}(\phi_{IG} + 1.5\Delta x) - \phi_{IG}\boldsymbol{u}_G}{1.5\Delta x} \tag{7.86}$$

Similarly, the velocity at the ghost points with respect to the liquid phase can also be calculated by solving Eqs. (7.82)–(7.85).

Calculation of the temperature field in the ghost fluid region:
The ghost value for the temperature at IG is calculated such that the jump condition in the heat flux given by Eq. (7.74) is satisfied. The jump in heat flux between the gaseous and the liquid phase is cast in the following form:

$$-k_g \left.\frac{\partial T}{\partial n}\right|_g + k_l \left.\frac{\partial T}{\partial n}\right|_l = \left[\dot{q}''_{\text{cond}}\right] \tag{7.87}$$

where k_g and k_l are the thermal conductivity of the gas and the liquid, respectively, at the interface. $\left(\frac{\partial T}{\partial n}\right)_g$ and $\left(\frac{\partial T}{\partial n}\right)_l$ are the thermal gradients in the gaseous and the liquid phase at the interface, in the direction normal to the interface. For a typical ghost point IG, shown in Fig. 7.3a, $\left(\frac{\partial T}{\partial n}\right)_g$ and $\left(\frac{\partial T}{\partial n}\right)_l$ are estimated from the following relations:

$$\left.\frac{\partial T}{\partial n}\right|_g = \frac{T_G - T_{I,g}}{1.5\Delta x} \tag{7.88}$$

$$\left.\frac{\partial T}{\partial n}\right|_l = -\frac{T_L - T_{I,l}}{1.5\Delta x} \tag{7.89}$$

where T_G and T_L are the temperature at the points G and L in Fig. 7.3a. Similar to the velocity components, T_G and T_L are estimated from the temperature at the nearest four grid points using bilinear interpolation. $T_{I,g}$ and $T_{I,l}$ are the temperature of the gaseous and liquid phases, respectively, at the interface. The jump in temperature at the interface is given by:

$$T_{I,g} - T_{I,l} = [\text{T}_I] \tag{7.90}$$

In this work, the temperature is assumed to be continuous at the interface. Therefore, $[\text{T}_I] = 0$.

Equations (7.88) and (7.89) are substituted in Eq. (7.87) to obtain:

$$-k_g \frac{T_G - T_{I,g}}{1.5\Delta x} - k_l \frac{T_L - T_{I,l}}{1.5\Delta x} = \left[\dot{q}''_{\text{cond}}\right] \tag{7.91}$$

Equations (7.90) and (7.91) are solved to obtain $T_{I,g}$ and $T_{I,l}$ as given below:

$$T_{I,g} = \frac{k_g T_G + k_l T_L + k_l[\text{T}_I] + 1.5\Delta x \left[\dot{q}''_{\text{cond}}\right]}{k_g + k_l} \tag{7.92}$$

$$T_{I,l} = \frac{k_g T_G + k_l T_L - k_g [T_I] + 1.5 \Delta x [\dot{q}''_{\text{cond}}]}{k_g + k_l} \qquad (7.93)$$

Once $T_{I,g}$ and $T_{I,l}$ are obtained, the ghost value of the temperature at *IG*, $T_G|_{\text{ghost}}$, is obtained by linear extrapolation:

$$T_{IG}|_{\text{ghost}} = \frac{T_{I,g}(\phi_{IG} + 1.5\Delta x) - \phi_{IG} T_G}{1.5\Delta x} \qquad (7.94)$$

Further detail of the current GFM can be found in Das and UdayKumar (2019).

7.3 Results and Discussion

The above numerical framework has been validated against several benchmark experimental and numerical studies in the previous work (Sambasivan and UdayKumar 2009; Shiv Kumar and UdayKumar 2009; Das 2017; Das et al. 2018a, b). In this section, we demonstrate the extent of the capabilities of the current sharp-interface methods in solving high-speed multi-material flow problems through the following numerical example involving fluid–solid, fluid–fluid, solid–solid, and solid–void interfaces.

7.3.1 Fluid–Rigid Solid Interface: Shock-Induced Lift-off of a Rigid Cylinder in a Shock Tube

A numerical study of shock-induced lift-off of a rigid cylinder is performed using the current method (Das 2017). The trajectory of the center of the cylinder calculated from the current calculations is compared with a benchmark result. The length of the computational domain is selected as the reference length scale and is taken to be 1.0. The height of the domain is 0.2 and the diameter of the cylinder is 0.1 non-dimensional units. The cylinder center is initially at (0.15, 0.05), i.e., the cylinder is placed close to the bottom wall of the shock tube. The non-dimensional values of the pressure and density of the un-shocked fluid are 1.4 and 1, respectively. The non-dimensionalized density of the cylinder is 10.77. The Reynolds number calculated based on the flow conditions behind the traveling shock wave is 240. A shock wave of Ma = 3.0 is located initially at $x = 0.08$ and is allowed to evolve until time $t = 0.3$ s. A reflective boundary condition is applied at the top and the bottom edges of the computation domain. Neumann boundary condition is applied at the east and the west edges of the computation domain. In this study, a uniform Cartesian grid is used. Five different grid resolutions are considered, corresponding to 50, 100, 150, 200, and 400 points across diameter for the grid convergence study. The numerical

Schlieren plots presented in Fig. 7.4 are obtained from the mesh with a grid resolution of 200 points across the diameter of the cylinder.

The numerical Schlieren fields computed at different time instances ($t = 0.0, 0.1, 0.3$ s) are shown in Fig. 7.4. As the flow evolves, the incident shock interacts with the cylinder and reflects from the cylinder surface. The reflected shock travels outward from the cylinder surface and interacts with the bottom wall. The shock wave reflected from the bottom wall of the computational domain interacts with the cylinder again, producing a non-zero lift on the cylinder. The non-zero lift causes the cylinder to move up from the bottom edge of the computational domain. The locus of the center of the moving cylinder is compared with the benchmark results (Shiv Kumar and UdayKumar 2009; Meyers 1994) in Fig. 7.5. The trajectory of the cylinder center obtained from the current study is in good agreement with the results of previous studies. It is also observed that the lift-off height of the cylinder is somewhat lower in the current viscous flow simulation, i.e., viscous effects suppress the lift-off of the

a) $t = 0.0s$

b) $t = 0.1s$

c) $t = 0.3s$
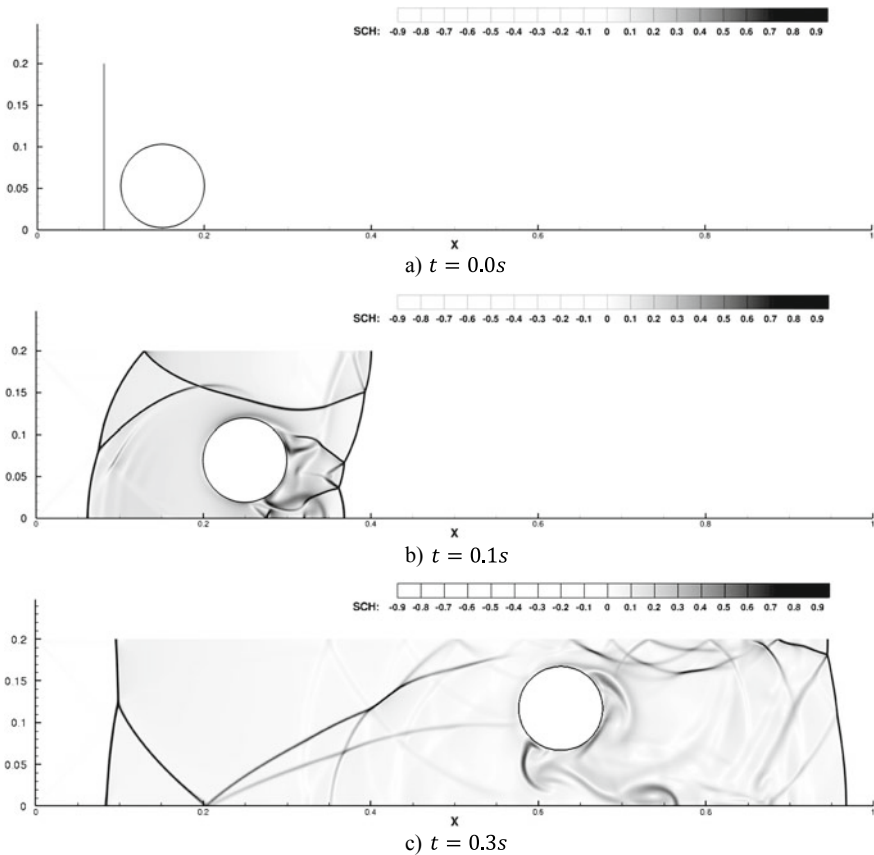
Fig. 7.4   Shock-induced ($M_s = 3.0$) lift-off of a rigid cylinder in shock tube
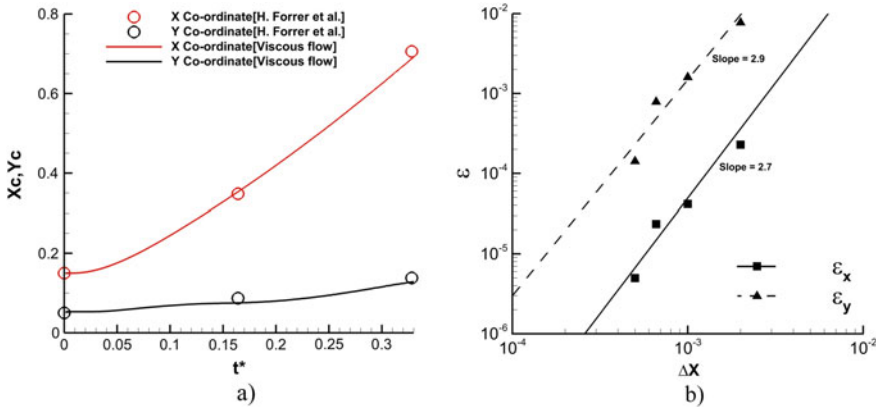
Fig. 7.5 **a** Locus of the center of the rigid cylinder during the shock-induced lift-off. **b** The decreasing L_2 error in the locus of the cylinder with grid refinement

cylinder. This effect is modest in the present case since the length over which the lift-off occurs is small. Thus, although the flow features differ noticeably between the viscous and inviscid cases, the differences in the particle motion are not significant for the current cylinder lift-off problem, at least for the duration of the simulation (Fig. 7.5).

A convergence study is performed for the above moving boundary problem; the convergence evaluation is based on the errors in tracking the locus of the cylinder center. The L_2 error in the locus of the cylinder is computed from:

$$
\varepsilon = \sqrt{\frac{\int_0^T \left(x_{c_i}^{\text{fine grid}} - x_{c_i}^{\text{Coarse grid}}\right)^2 \mathrm{d}t}{\int_0^T \left(x_{c_i}^{\text{fine grid}}\right)^2 \mathrm{d}t}} \tag{7.95}
$$

The error is seen to monotonically decrease with grid refinement in Fig. 7.5a.

Results obtained from the simulation of cylinder lift-off caused by shock impingement in a shock tube show that the current GFM is adequate for viscous simulations of moving boundary problems in supersonic flow.

7.3.2 Fluid–Rigid Solid Interactions: Mach 5 Shock Interaction with a Cluster of Particles

A resolved simulation of shock interaction with a cluster of randomly arranged cylindrical particles is demonstrated. In this simulation, the shock Mach number (M_s) is 5. A cluster of 62 randomly arranged aluminum particles of uniform diameter is used in this simulation. The volume fraction (ϕ) of the particles in the cluster is

5%. Reynolds number of the post-shock incoming flow with respect to each particle (Re_D) is 1000.

A uniform Cartesian grid used in the current calculation. The solid–fluid interfaces of the particles are tracked sharply using the current levelset-based approach. No-slip boundary condition is applied at the interface. The particles in this calculation are resolved using 100 mesh points across the diameter to capture the viscous boundary layer on the particles. The diameter of the particles (D) is selected as the characteristic length scale in this calculation. The initial configuration of the particle cloud immersed in a quiescent fluid is shown in Fig. 7.6a. Outflow boundary conditions are applied on all sides of the computational domain.

The sequence of numerical Schlieren in Fig. 7.6a–c shows the evolution of the unsteady flow field and the intricate shock structures during the interaction of incoming shock waves with the particles. As the incident shock interacts with the particle cluster, the reflections of the incident shock from the front row of the particles coalesce to form an effectively planar reflected shock, as seen in Fig. 7.6b, c. A part of the incident shock is also transmitted through the cluster of particles. The reflected and transmitted shock waves are seen in Fig. 7.6c. The transmitted shock loses its strength as it travels through the cluster of particles. The attenuation of the strength of the transmitted shock wave has been observed previously by Chaudhury et al. (2013).

As the transmitted shock wave propagates through the cluster, multiple internal reflections of the shocks lead to an unsteady flow field. The vorticity contour plot of the shocked flow field at $t * \frac{U_s}{D} = 57.0$ in Fig. 7.7 exhibits this unsteadiness. Baroclinic vortices generated in the slip lines combine with wake vortices caused by separated shear layers form the coherent structures observed in the vorticity contour plot. Vorticity concentrations are also seen in inviscid flow calculations of shocks traversing particle clusters (Das 2017; Regele et al. 2014). In the present case, viscous effects augment the inviscid vorticity generation mechanisms leading to increased magnitudes of vorticity in the cluster (Das 2017).

Significant movement of the particles during the interaction with the incoming shock wave is not observed in the current simulation. This is because the timescale of the current simulation is significantly smaller than the timescale of the movement of the particles (Das 2017; Mehta et al. 2016). However, it is worth mentioning that the particle cluster gets compressed inhomogeneously during the interaction with the shock. The sequence of numerical Schlieren in Fig. 7.7 shows that the displacement of the particles in the downstream part of the cloud is less than the particles in the front of the cloud. As the shock passes over the cloud, the particles located at the leading edge begin to equilibrate with the flow even before the shock has reached the downstream end of the cloud. Owing to this, the particles at the front-end start moving before the shock reaches the trailing end of the cloud. This leads to enhanced clustering at the leading edge of the cloud, i.e., the local volume fraction of the particles at the front-end of the cloud becomes higher relative to the rear-end. Therefore, even within the short period of the shock passage, movement of the particles changes the local solid volume fraction in the cloud.

a) $t * U_s/D = 0.0$

b) $t * \frac{U_s}{D} \sim 20.0$

c) $t = 57.0$
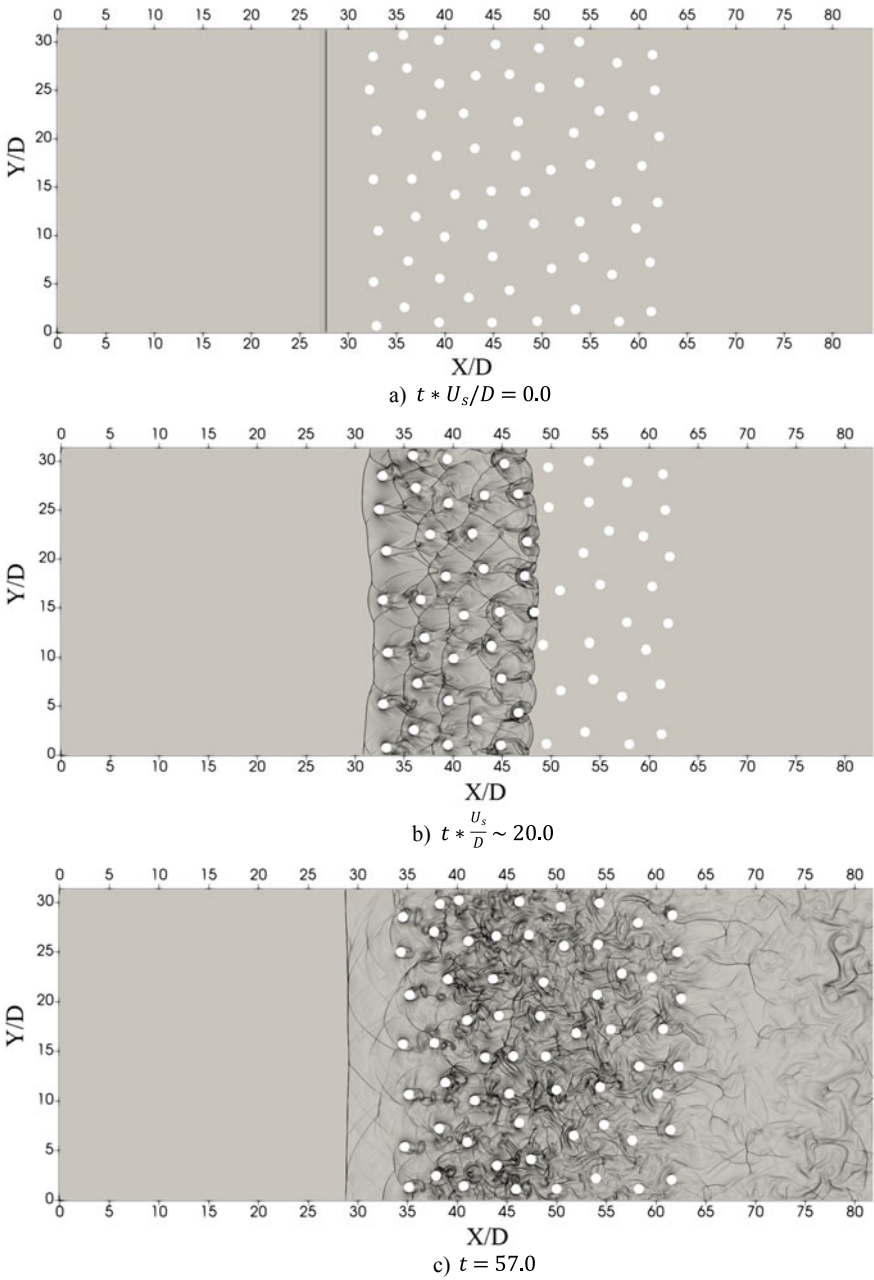
Fig. 7.6 Mach 5 shock interaction with a cluster of 62 rigid cylindrical particles
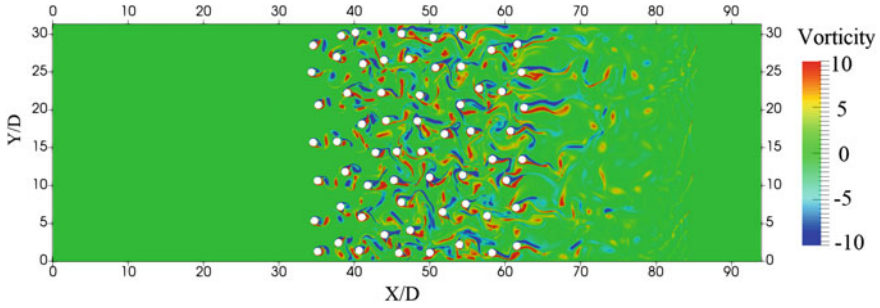
Fig. 7.7 Vorticity contours during Mach 5 shock interaction with a cluster of particles of 10% volume fraction

The results obtained from the current simulation show that the levelset-based approach in conjunction with the current GFM can capture the intricate features of the flow fields, such as the viscous boundary layer over the particles and the movement of the particles due to shock interaction. The current results and the previous studies (Khan and Huang 1995; Massoni et al. 1999; Houim and Kuo 2013) have shown that the current levelset-based approach is suitable for studying shock interaction with particle clouds through resolved simulations.

7.3.3   Gas–Liquid Interfaces: Mach 3.5 Shock Interaction with an Aluminum Droplet

The shock-induced combustion of a cylindrical droplet is studied using the current levelset-based sharp-interface method. For this study, the interaction of a Mach 3.5 shock wave with a cylindrical aluminum droplet of 4 μm in diameter is simulated. The initial computational setup for the simulation is shown in Fig. 7.8. Reflective

Fig. 7.8 Initial condition for 2D simulation of Mach 3.5 shock interaction with an aluminum droplet of 4 micron in diameter
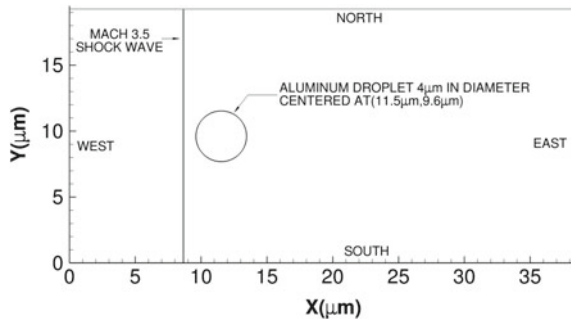
boundary conditions are used at the north and the south boundaries of the computational domain. An outflow boundary condition is used at the east and the west boundaries. The initial conditions for the simulation are as in Table 7.1.

The vaporization of the aluminum droplet at the surface and the combustion of the evaporated aluminum in the air are modeled in this calculation. An 11-step reduced-order reaction model for aluminum combustion in the air is used for this current calculation (Huang et al. 2009). The material properties for the gas and the liquid phases such as viscosity, thermal conductivity, and surface tension used in the current simulation can be found in Houim (2011). With the given values for the material properties and the flow conditions, the non-dimensional numbers are $Re_D =$ 1000 and $We_D = 31.56$. The grid resolution of 200 mesh points across the diameter is used for this study.

The interaction of Mach 3.5 shock with the aluminum droplet is shown through multiple snapshots of numerical Schlieren and pressure contours in Fig. 7.9. The initial interaction of the incident shock with the droplet is demonstrated in Fig. 7.9a–c. The high temperature and the impulsive vaporization of the molten aluminum droplet initiate a shock wave at the droplet surface as seen in Fig. 7.9a. The interaction of the incident shock with the gas–liquid interface produces a reflected shock in the gas and a transmitted shock in the liquid. The reflected and transmitted waves are seen in Fig. 7.9a. The transmitted wave travels faster through the liquid than the incident wave in the air as the speed of sound is higher in the liquid than in air. The transmitted shock wave travels further through the droplet and reaches the gas–liquid interface at the leeward side of the droplet, as shown in Fig. 7.9b. Figure 7.9c shows that the transmitted wave reflects back from the interface at the leeward end into the droplet as a strong expansion wave. Therefore, the numerical Schlieren and the pressure contours in Fig. 7.9a–c demonstrate that the physical behavior of nonlinear wave interaction with the gas–liquid interface is captured by the current sharp-interface method. The higher pressure observed within the droplet is due to the effect of surface tension. This shows that the current GFM incorporates the effects of surface tension while accurately propagating the characteristic waves from one medium to another at the interface.

Figure 7.9d, e show, as the flow evolves further, the shock wave travels past the droplet and the droplet starts to deform. The vaporized aluminum accumulated in the wake starts to react with air in the wake of the droplet. The chemical reaction induces strong unsteadiness and asymmetry in the wake even at the low Re_D. The contours of temperature and the species mass fractions are shown in Fig. 7.10. Figure 7.10a shows that an unsteady diffusion flame forms in the wake of the droplet. The highest temperature occurs in the shear layers, close to the boundary layer detachment points behind the droplets. This is because of the high concentration of the aluminum vapor in the shear layer behind the droplets, as seen in Fig. 7.10b. The aluminum vapor generated at the front side droplet surface is mostly contained within the thin boundary layer on the droplet surface. As the boundary layer detaches from the surface at the leeward side of the droplet, the aluminum vapor accumulated in the boundary layer flows into the post-detachment shear layer. However, Fig. 7.10b shows that there in a very little amount of aluminum vapor in the recirculation region

a) $t * U_s/D = 0.6$

b) $t * U_s/D = 0.7$

c) $t * U_s/D = 0.8$

d) $t * U_s/D = 3.0$

e) $t * U_s/D = 13.0$
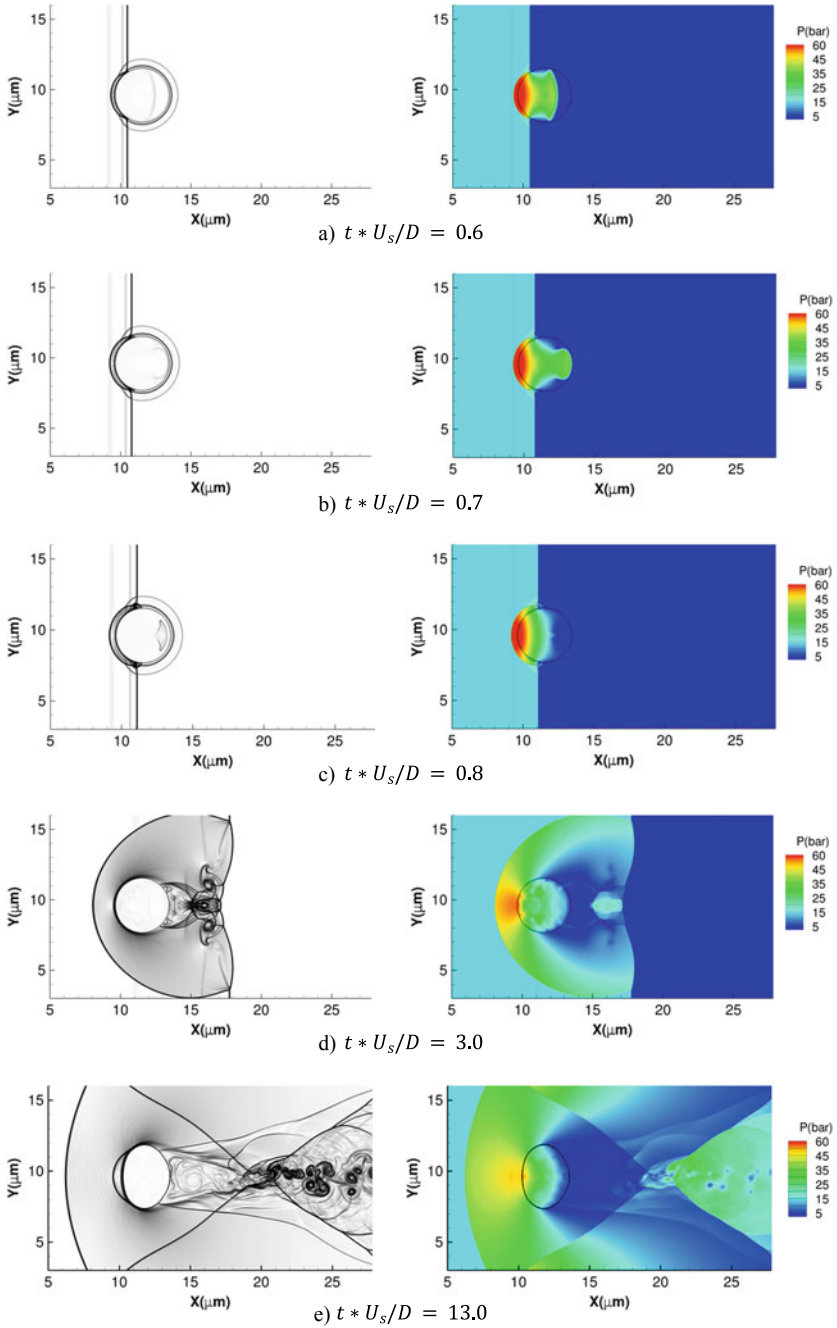
Fig. 7.9 Sequence of contour plot obtained from the simulation of Mach 3.5 shock interacting with and aluminum droplet (Red = 1000). The left column shows the numerical schlieren images. Pressure contours are shown in the right column
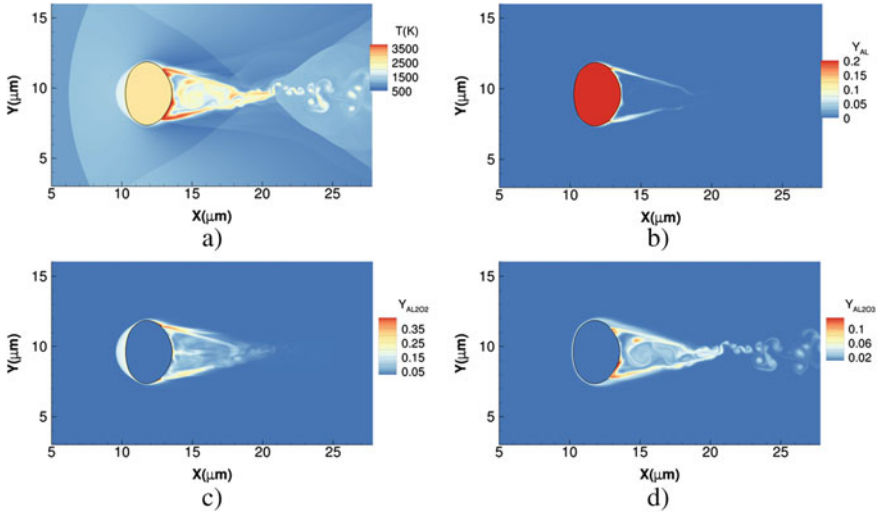
Fig. 7.10 Contours of temperature (**a**) and mass fractions of aluminum vapor (**b**), Al_2O_2 (**c**), and Al_2O_3 (**d**) during the Mach 3.5 shock-induced combustion of an aluminum droplet

behind the droplet. This is due to the fact that most of the evaporated aluminum gets oxidized in the shear layer. The evaporated aluminum in the shear layer reacts with the oxygen in the freestream and the high-temperature diffusion flame is formed. The combustion products such as Al_2O_2 and Al_2O_3 flow into the recirculation region behind the droplets. Figure 7.10c, d shows the accumulations of the combustion products within the recirculation bubble.

The results presented in this section show that the current sharp-interface method coupled with the compressible reacting flow solver successfully resolves the nuances of droplet combustion in a shocked flow. The current GFM allows the characteristic waves to travel across the gas–liquid interfaces without generating numerical artifacts. The effects of surface tension and vaporization at the liquid surface are also incorporated using the current sharp-interface method. The reacting flow simulation shows that the current method is suitable for interface-resolved simulation of droplet combustion in shocked flows.

7.3.4 Solid–Void Interactions: Reactive Pore Collapse in HMX Under 1000 m/s Shock Load

The capability of the current framework to handle shock-induced chemical reaction is analyzed by studying the initiation and growth of reaction in a porous energetic material, HMX. In porous energetic materials, the collapse of pores under shock load leads to the formation of localized heated regions called hotspots (Field John
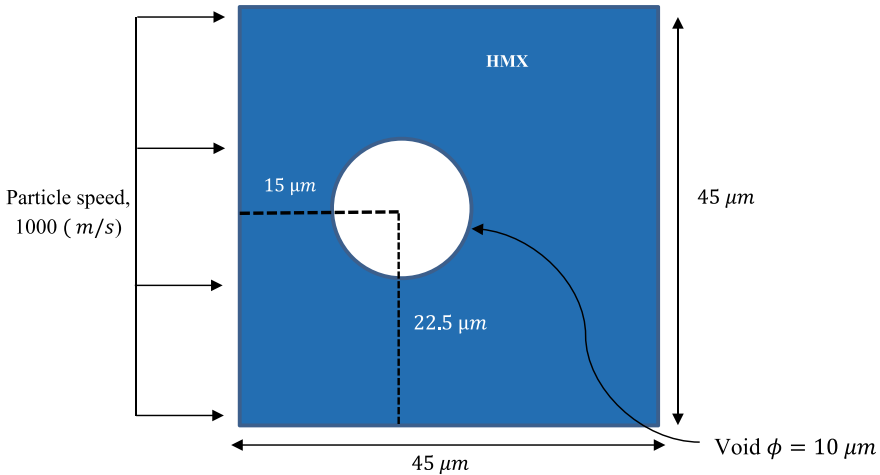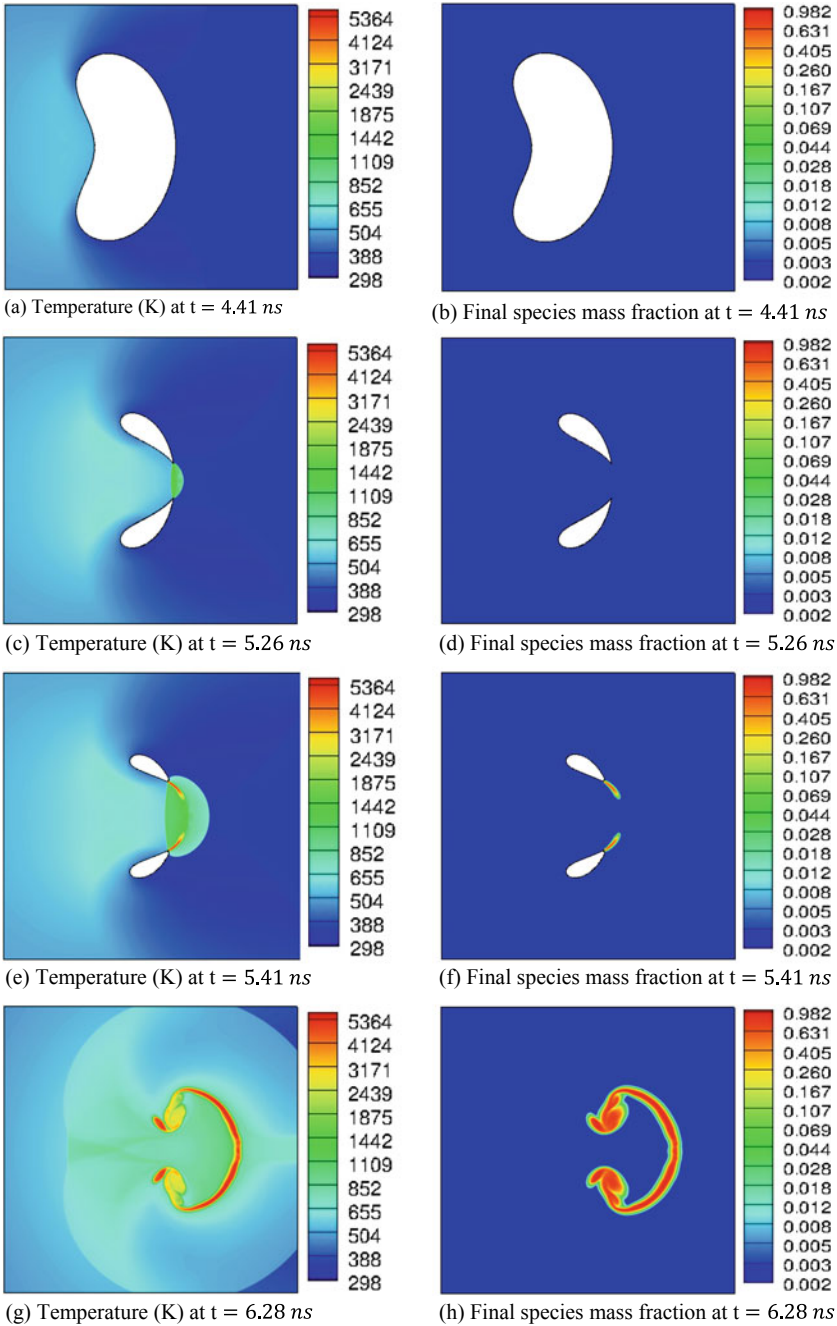
Fig. 7.11 Cylindrical void of diameter 10 μm embedded in the HMX domain of size 45×45 μm shock load is applied as a velocity boundary condition in the form of a pulse of duration 3 ns. The east, south, and north faces of the domain are supplied with outlet boundary condition

1992). Depending on the temperature and size of the hotspot, chemical reactions can initiate and grow in the material. To understand the behavior of hotspots in porous HMX, reactive pore collapse simulations are performed for a 10 μm diameter pore impacted under a sustained shock of particle speed, 1000 m/s as shown in Fig. 7.11. Shock load is applied from the west face of the domain boundary. The east, north, and south boundaries are supplied with zero-gradient boundary conditions. The reaction initiation in the hotspot is modeled using Arrhenius kinetics-based three steps decomposition mechanism proposed by Tarver et al. (1996). The reaction initiation in the hotspot region leads to the decomposition of solid HMX to gaseous reaction products. To define the mixture pressure, the Birch–Murnaghan equation of state is used for the HMX and JWL equation of state is implemented for the final gaseous products.

Figure 7.12 shows the temperature and mass fraction of the final gaseous species contours obtained from the reactive pore collapse analysis. Figure 7.12c, d shows that material jet impact forms near the pore interface and leads to the formation of the blast wave along with the symmetrical secondary lobes. The blast wave leads to the collapse of the secondary lobes is seen in Fig. 7.12f. The temperature at the lobe collapse locations is high enough to initiate the chemical reaction (Fig. 7.12f). As the collapse of the secondary lobes progresses, a further rise in temperature takes place which is also augmented by energy released because of chemical reactions. Eventually, the complete collapse of the secondary lobes takes place and ignites the HMX material at the secondary lobe locations. The reaction zone grows from the lobe collapse locations to its surrounding under the combined influence of convection and diffusion. It is interesting to note that for the applied shock, the rise in the temperature

(a) Temperature (K) at t = 4.41 ns

(b) Final species mass fraction at t = 4.41 ns

(c) Temperature (K) at t = 5.26 ns

(d) Final species mass fraction at t = 5.26 ns

(e) Temperature (K) at t = 5.41 ns

(f) Final species mass fraction at t = 5.41 ns

(g) Temperature (K) at t = 6.28 ns

(h) Final species mass fraction at t = 6.28 ns

Fig. 7.12 Contour plots of temperature and mass fraction of the final species at different instances of time for reactive single void collapse analysis under shock loading of 1000 m/s. The grid size for the current simulation corresponds to 700 grid points across the void diameter of 10 μm

because of the initial jet impact is not enough to initiate the reaction. Instead, reaction initiates at the offset locations where secondary lobes are collapsed.

The current analysis shows the numerical framework can predict the initiation and growth of chemical reaction in porous energetic materials.

7.3.5 Solid–Solid Interactions: Shock Compaction of Metallic Particles Mixture

To demonstrate the ability of the current framework to handle compaction of large clusters of particles, shock compaction of Ni/Al metallic mixtures is performed. The numerical setup consists of a collection of spherical particles (Al-Ni mixture) impacted by a copper flyer plate at the velocity of 1 km/s. The volume fraction of particles is 60%, with the rest being void space. The particles have a diameter of 20 μm and a frictionless contact is imposed at the interface. The computational domain is 200 $\times$ 200 μm. The north and south domain boundaries are frictionless walls. The copper plate is modeled as a piston that extends indefinitely to the left. Thus, the west boundary is modeled with a constant velocity of 1 km/s. The mesh size is set to have 50 grid cells across the diameter of a particle. Each particle interface is modeled by a separate levelset function to allow for full contact-separation treatment (Rai et al. 2014). Frictionless contact (sliding) condition is imposed between all particles.

Figure 7.13 shows the density and temperature profiles at time $t = 40$ ns, $t = 70$ n, and $t = 90$ ns. As seen in the figure, the Al particles undergo more deformation than the Ni particles. The nickel particles tend to form clusters. This preferential flow of Al through the Ni matrix and the clustering of Ni are observed in experiments (Eakins and Thadhani 2008) as well as in other simulations (Eakins and Thadhani 2008). As can be observed, the focused flows of aluminum pinched between other particles create jets of material with localized high temperature and velocity. The flows cause the formation of small breakaway particulate material that detaches from their original particle, as observed in previous simulations using CTH (Eakins and Thadhani 2008). The particle fragments are at high temperature and can be ejected from compacted particles with high velocity.

Vortex flows are also observed in our calculations, as in other experimental and simulation work (Nesterenko et al. 1994; Tamura and Horie 1998). A detailed view at time $t = 74$ ns is presented in Fig. 7.14. Aluminum particles form a focused flow that encounters nickel particles. The aluminum is melted and swirls around a void forming a vortex pattern. This vortex is mostly composed of aluminum; the deformability of globular Ni is too low to effectively mix with Al in this vortex, which explains the inertness of Ni-Al mixtures (Eakins and Thadhani 2009). Thus, despite the high mixing of the particles in such vortical flows, in mixtures with large differences in deformability (such as in Ni-Al systems), vortical flows do not contribute to the triggering of the chemical reaction. The compaction of spherical-shaped particles
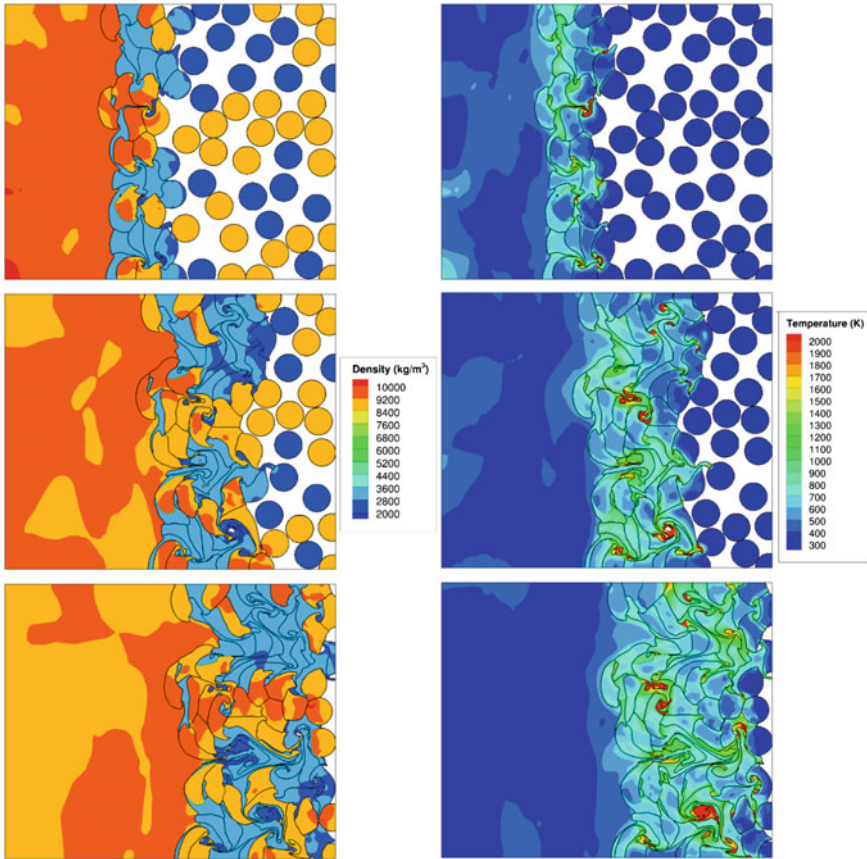
Fig. 7.13 Density and temperature fields for a Ni/Al mixture impacted by a copper flyer plate at 1 km/s at time $t = 40$ ns, $t = 70$ ns, and $t = 90$ ns

was found to present less contact area and mass mixing between aluminum and nickel particles, and thus to be less sensitive to shock-initiated chemical reaction (Eakins and Thadhani 2008). Flake Ni particles mixed with Al were found to yield more intimate mixing (Eakins and Thadhani 2006). Thus, particle morphology plays a significant role in initiating reactions.

Therefore, the current analysis shows that the current Eulerian framework can efficiently handle contact and impact situation leading to the large deformation of deformable solids that exhibit elastoplastic behavior under shock loading.
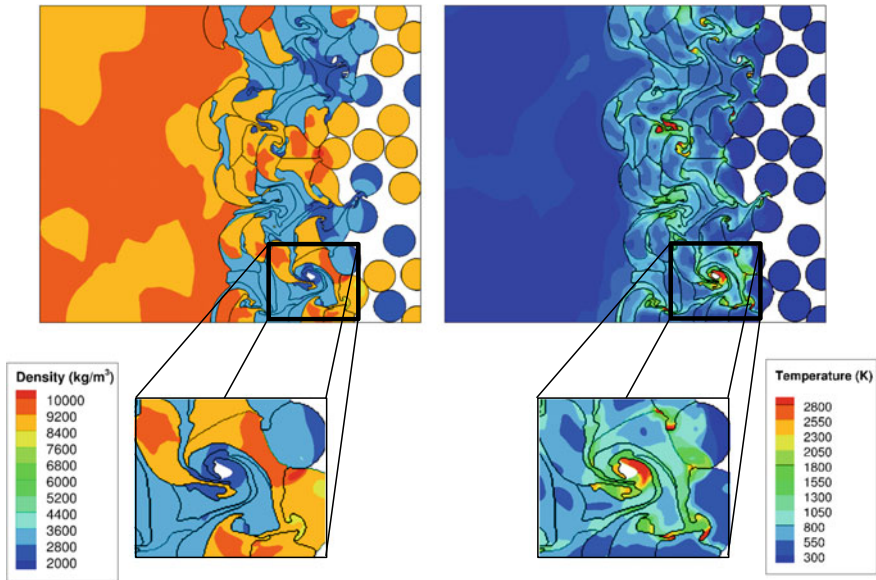
Fig. 7.14 Density and temperature fields for a Ni/Al mixture impacted by a copper flyer plate at 1 km/s at time $t = 74$ ns. Detail of the particle compaction

7.4   Conclusions

A versatile sharp-interface Eulerian method is presented for the interface-resolved simulations of high-speed multi-material flows. The levelset method is used to track the large deformation of the material interfaces. A modified ghost fluid method is used to supply the appropriate boundary conditions to the corresponding materials at the interfaces. The current method allows for a broad-range of high-speed multi-material flow problems involving interactions between solid and fluid phases in a generic Cartesian grid-based Eulerian framework.

The generality of the current framework is owing to the hyperbolic nature of the governing equations and the sharp-interface method for capturing the complex interfacial dynamics. The hypo-elastic model for stress-train relations under the high-strain rate assumptions allows us to cast the governing equations for solid materials in an Eulerian framework. Therefore, a unified Eulerian framework is used for solving the governing equation for both solid and fluid phases under high-speed conditions.

The multi-material interfaces embedded in the fixed Eulerian grid are tracked sharply using levelset methods. The levelset method allows us to track extreme topological changes in the material interfaces with ease and robustness. The simulations presented in the results section demonstrate that the levelset method can be used to track extreme deformation of multiple closed interfaces within a single simulation. The levelset-based sharp-interface tracking coupled with current GFM is used to couple the field variables of different materials at the interfaces accurately. Different

interfacial flow phenomenon such as nonlinear wave interaction with the interfaces, the effects of phase change and surface tension at the interface are modeled using the current GFM. The current GFM is suitable for imposing the appropriate boundary conditions at the interfaces separating different materials and/or phases.

The capability of the current framework to handle large deformation, phase change, and chemical reactions is demonstrated using a wide variety of problems involving high-speed multi-material interactions between the solid, liquid, and gaseous phases. The interactions of rigid solid–fluid, fluid–fluid, and deformable solid–void interfaces are demonstrated through three different problems in the results section, i.e., shock-induced lift-off a rigid cylinder and combustion of aluminum droplet under a Mach 3.5 shock, and pore collapse-induced reaction initiation in energetic materials under shock load. Shock interactions with multi-material interfaces are captured accurately in the current method. The simulation of shock interactions with an aluminum droplet demonstrates that the current Riemann solver-based GFM allows the nonlinear wave to travel across the gas–liquid interfaces without incurring any artificial numerical artifact. The sharp-interface multiphase framework is shown to efficiently handle the large deformation involved in the collapse of the pore in HMX to form hotspot. The multiphase framework allows to track the reaction initiation and expansion of the reaction products from the hotspots to the surrounding involving the decomposition of solid HMX. Therefore, the three problems demonstrate the robustness of the sharp-interface multiphase framework to handle large deformation, phase change, and chemical reactions in wide variety of materials.

The robustness and efficiency of the current framework to handle process scale simulations are demonstrated by solving two problems involving many particles, i.e., shock interaction of cluster of rigid particles and the compaction of Ni/Al metallic powder under shock load. Each particle is defined using the narrow-band levelset approach. The simulations of shock interaction of particle cluster demonstrate the capabilities of the current numerical method to perform resolved simulations of particle-laden flows. The current method is used in Das et al. (2018) to develop surrogate models for drag on particles in shocked flows from resolved 3D simulations. In the simulation of shock-induced compaction of Ni/Al powder, the definition of the particles using different levelsets allows to model the physics governing the compaction between the Ni/Al particles accurately. The sharp-interface tracking of the particles is shown to handle the localized extreme deformation situations efficiently that arise during the compaction of the metallic powder bed. Therefore, these simulations demonstrate the capability of the current framework to perform large scale simulations relevant to real-world engineering applications.

References

Artemieva NA, Shuvalov VV (2008) Numerical simulation of high-velocity impact ejecta following falls of comets and asteroids onto the Moon. Sol Syst Res 42(4):329–334

Boiko VM et al (1997) Shock wave interaction with a cloud of particles. Shock Waves 7(5):275–285

Burcat's Thermodynamic Data

Bürger D et al (2012) Ballistic impact simulation of an armour-piercing projectile on hybrid ceramic/fiber reinforced composite armours. Int J Impact Eng 43:63–77

Chaudhuri A et al (2013) Numerical study of shock-wave mitigation through matrices of solid obstacles. Shock Waves 23(1):91–101

Das P et al (2017) A sharp interface Cartesian grid method for viscous simulation of shocked particle-laden flows. Int J Comput Fluid Dyn 31(6–8):1–23

Das P, UdayKumar HS (2019) A sharp-interface method for the simulation of shock-induced vaporization of droplets. J Comp Phys (in press)

Das P et al (2018a) Metamodels for interphase heat transfer from mesoscale simulations of Shock-Cylinder Interactions. AIAA Journal 56(10):3975–3987

Das P et al (2018b) Strategies for efficient machine learning of surrogate drag models from three-dimensional mesoscale computations of shocked particulate flows. Int J Multiph Flow 108:51–68

Dongmo E, Wenzelburger M, Gadow R (2008) Analysis and optimization of the HVOF process by combined experimental and numerical approaches. Surf Coat Technol 202(18):4470–4478

Eakins D, Thadhani NN (2006) Shock-induced reaction in a flake nickel + spherical aluminum powder mixture. J Appl Phys 100(11):113521

Eakins DE, Thadhani NN (2008a) The shock-densification behavior of three distinct Ni + Al powder mixtures. Appl Phys Lett 92(11):111903

Eakins DE, Thadhani NN (2008b) Mesoscale simulation of the configuration-dependent shock-compression response of Ni + Al powder mixtures. Acta Mater 56(7):1496–1510

Eakins DE, Thadhani NN (2009) Shock compression of reactive powder mixtures. Int Mater Rev 54(4):181–213

Fedkiw RP et al (1999) A non-oscillatory Eulerian approach to interfaces in multimaterial flows (the Ghost Fluid Method). J Comput Phys 152(2):457–492

Field John E et al (1992) Hot-spot ignition mechanisms for explosives and propellants. Philos Trans R Soc London Ser A: Phys Eng Sci 339(1654):269–283

Gottlieb S, Shu C-W (1998) Total variation diminishing Runge-Kutta schemes. Math Comput Am Math Soc 67(221):73–85

Hirt CW, Nichols BD (1981) Volume of fluid (VOF) method for the dynamics of free boundaries. J Comput Phys 39(1):201–225

Houim RW (2011) Modeling the influence of shock waves on the combustion of aluminum droplets

Houim RW, Kuo KK (2013) A ghost fluid method for compressible reacting flows with phase change. J Comput Phys 235:865–900

Huang Y et al (2009) Effect of particle size on combustion of aluminum particle dust in air. Combust Flame 156(1):5–13

Jamaluddin AR et al (2011) The collapse of single bubbles and approximation of the far-field acoustic emissions for cavitation induced by shock wave lithotripsy. J Fluid Mech 677:305–341

Jiang G-S, Shu C-W (1996) Efficient implementation of weighted ENO schemes. J Comput Phys 126(1):202–228

Khan A, Huang S (1995) Continuum theory of plasticity. Wiley, New York

Liu TG, Khoo BC, Wang CW (2005) The ghost fluid method for compressible gas–water simulation. J Comput Phys 204(1):193–221

Marusich TD, Ortiz M (1995) Modelling and simulation of high-speed machining. Int J Numer Meth Eng 38(21):3675–3694

Massoni J et al (1999) A mechanistic model for shock initiation of solid explosives. Phys Fluids 11(3):710–736

Mayer W, Tamura H (1996) Propellant injection in a liquid oxygen/gaseous hydrogen rocket engine. J Propul Power 12(6):1137–1147

Mehta Y et al (2016) Shock interaction with three-dimensional face centered cubic array of particles. Phys Rev Fluids 1(5):054202

Meyers MA (1994) Dynamic behavior of materials. Wiley, New York

Mousel J (2012) A massively parallel adaptive sharp interface solver with application to mechanical heart valve simulations. Theses and Dissertations

Nesterenko VF et al (1994) Controlled high-rate localized shear in porous reactive media. Appl Phys Lett 65(24):3069–3071

Osher S, Sethian JA (1988) Fronts propagating with curvature-dependent speed: algorithms based on Hamilton-Jacobi formulations. J Comput Phys 79(1):12–49

Ponthot JP (2002) Unified stress update algorithms for the numerical simulation of large deformation elasto-plastic and elasto-viscoplastic processes. Int J Plast 18(1):91–126

Powell OA et al (2001) Development of hydrocarbon-fueled scramjet engines: the hypersonic technology (HyTech) program. J Propul Power 17(6):1170–1176

Rai NK, Kapahi A, Udaykumar HS (2014) Treatment of contact separation in Eulerian high-speed multimaterial dynamic simulations. Int J Numer Meth Eng 100(11):793–813

Regele JD et al (2014) Unsteady effects in dense, high speed, particle laden flows. Int J Multiph Flow 61:1–13

Sambasivan SK, UdayKumar HS (2009) Ghost fluid method for strong shock interactions Part 1: fluid-fluid interfaces. AIAA J 47(12):2907–2922

Sambasivan S, Kapahi A, Udaykumar HS (2013) Simulation of high speed impact, penetration and fragmentation problems on locally refined Cartesian grids. J Comput Phys 235:334–370

Scardovelli R, Zaleski S (2000) Analytical relations connecting linear interfaces and volume fractions in rectangular grids. J Comput Phys 164(1):228–237

Sethian JA, Smereka P (2003) Level set methods for fluid interfaces. Annu Rev Fluid Mech 35(1):341–372

Shiv Kumar S, UdayKumar HS (2009) Ghost fluid method for strong shock interactions Part 2: immersed solid boundaries. AIAA j 47(12):2923–2937

Shu C-W, Osher S (1989) Efficient implementation of essentially non-oscillatory shock-capturing schemes, II. In: Hussaini PMY , Leer PBV, Rosendale DJV (eds) Upwind and high-resolution schemes. Springer, Berlin, pp 328–374

Sussman M, Smereka P, Osher S (1994) A level set approach for computing solutions to incompressible two-phase flow. J Comput Phys 114(1):146–159

Sussman M et al (1998) An improved level set method for incompressible two-phase flows. Comput Fluids 27(5–6):663–680

Tamura S, Horie Y (1998) Discrete meso-dynamic simulation of thermal explosion in shear bands. J Appl Phys 84(7):3574–3580

Tarver CM, Chidester SK, Nichols AL (1996) critical conditions for impact- and shock-induced hot spots in solid explosives. J Phys Chem 100(14):5794–5799

Thadhani NN (1988) Shock compression processing of powders. Adv Mater Manuf Process 3(4):493–549

Unverdi SO, Tryggvason G (1992) A front-tracking method for viscous, incompressible, multi-fluid flows. J Comput Phys 100(1):25–37

Verwer JG, Sommeijer BP, Hundsdorfer W (2004) RKC time-stepping for advection—diffusion—reaction problems. J Comput Phys 201(1):61–79